



Calculation of predictions for non-identical particle correlations in heavy ions collisions at LHC energies from hydrodynamics-inspired models

MASTER OF SCIENCE THESIS

Author:
Mateusz Wojciech Gałażyn

Supervisor:
Prof. Adam Kisiel

Warsaw, 5th November 2014



Wyznaczenie przewidywań teoretycznych dla korelacji cząstek nieidentycznych w zderzeniach ciężkich jonów przy energiach LHC w modelach opartych na hydrodynamice

PRACA MAGISTERSKA

Autor:
Mateusz Wojciech Gałażyn

Promotor:
dr hab. inż. Adam Kisiel, prof. PW

Warszawa, 5 listopada 2014

Abstract

Streszczenie

Contents

| | | |
|----------|---|-----------|
| 1 | Theory of heavy ion collisions | 2 |
| 1.1 | The Standard Model | 2 |
| 1.2 | Quantum Chromodynamics | 3 |
| 1.2.1 | Quarks and gluons | 3 |
| 1.2.2 | Quantum Chromodynamics potential | 4 |
| 1.2.3 | The quark-gluon plasma | 6 |
| 1.3 | Relativistic heavy ion collisions | 7 |
| 1.3.1 | Stages of heavy ion collision | 7 |
| 1.3.2 | QGP signatures | 9 |
| 2 | Terminator model | 17 |
| 2.1 | (3+1)-dimensional viscous hydrodynamics | 17 |
| 2.2 | Statistical hadronization | 18 |
| 2.2.1 | Cooper-Frye formalism | 19 |
| 3 | Particle interferometry | 21 |
| 3.1 | HBT interferometry | 21 |
| 3.2 | Theoretical approach | 22 |
| 3.2.1 | Conventions used | 22 |
| 3.2.2 | Two particle wave function | 23 |
| 3.2.3 | Source emission function | 24 |
| 3.2.4 | Theoretical correlation function | 26 |
| 3.2.5 | Spherical harmonics decomposition of a correlation function | 27 |
| 3.3 | Experimental approach | 28 |
| 3.4 | Scaling of femtoscopic radii | 29 |
| 3.4.1 | Scaling in LCMS | 30 |
| 3.4.2 | Scaling in PRF | 30 |
| 4 | Results | 32 |
| 4.1 | Identical particles correlations | 32 |
| 4.1.1 | Spherical harmonics components | 32 |
| 4.1.2 | Centrality dependence of a correlation function | 36 |
| 4.1.3 | k_T dependence of a correlation function | 37 |

| | | |
|----|--|-----------|
| 34 | 4.2 Results of the fitting procedure | 38 |
| 35 | 4.2.1 Femtoscopic radii scaling with the transverse mass | 38 |
| 36 | 4.3 Discussion of results | 43 |
| 37 | 5 Summary | 44 |

³⁸ Introduction

³⁹ **Chapter 1**

⁴⁰ **Theory of heavy ion collisions**

⁴¹ **1.1 The Standard Model**

⁴² In the 1970s, a new theory of fundamental particles and their interaction
⁴³ emerged. A new concept, which concerns the electromagnetic, weak and strong
⁴⁴ nuclear interactions between known particles. This theory is called *The Standard
45 Model*. There are seventeen named particles in the standard model, organized
⁴⁶ into the chart shown below (Fig. 1.1). Fundamental particles are divided into
two families: *fermions* and *bosons*.

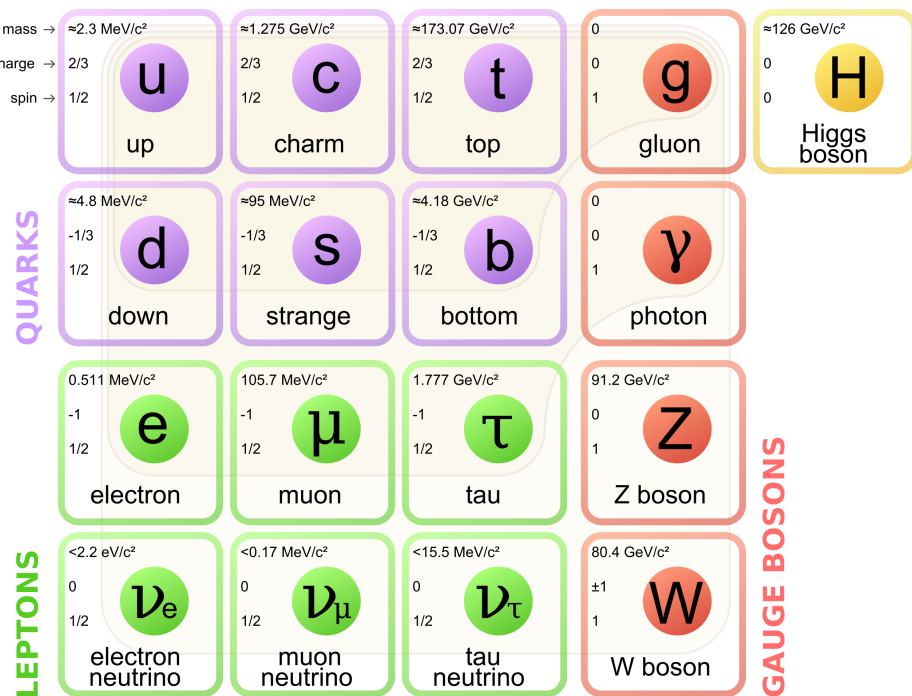


Figure 1.1: The Standard Model of elementary particles [1].

47 Fermions are the building blocks of matter. They are divided into two groups.
 48 Six of them, which must bind together are called *quarks*. Quarks are known to
 49 bind into doublets (*mesons*), triplets (*baryons*) and recently confirmed four-quark
 50 states.¹ Two of baryons, with the longest lifetimes, are forming a nucleus: a pro-
 51 ton and a neutron. A proton is build from two up quarks and one down, and
 52 neutron consists of two down quarks and one up. A proton is found to be a stable
 53 particle (at least it has a lifetime larger than 10^{35} years) and a free neutron has a
 54 mean lifetime about 8.8×10^2 s. Fermions, that can exist independently are called
 55 *leptons*. Neutrinos are a subgroup of leptons, which are only influenced by weak
 56 interaction. Fermions can be divided into three generations (three columns in
 57 the Figure 1.1). Generation I particles can combine into hadrons with the longest
 58 life spans. Generation II and III consists of unstable particles which form also
 59 unstable hadrons.

60 Bosons are force carriers. There are four fundamental forces: weak - respons-
 61 ible for radioactive decay, strong - coupling quarks into hadrons, electromagnetic
 62 - between charged particles and gravity - the weakest, which causes the attraction
 63 between particles with a mass. The Standard Model describes the first three. The
 64 weak force is mediated by W^\pm and Z^0 bosons, electromagnetic force is carried by
 65 photons γ and the carriers of a strong interaction are gluons g . The fifth boson is
 66 a Higgs boson which is responsible for giving other particles mass.

67 1.2 Quantum Chromodynamics

68 1.2.1 Quarks and gluons

69 Quarks interact with each other through the strong interaction. The mediator
 70 of this force is a *gluon* - a massless and chargeless particle. In the quantum chro-
 71 modynamics (QCD) - theory describing strong interaction - there are six types of
 72 "charges" (like electrical charges in the electrodynamics) called *colours*. The col-
 73 ours were introduced because some of the observed particles, like Δ^- , Δ^{++} and
 74 Ω^- appeared to consist of three quarks with the same flavour (ddd , uuu and sss
 75 respectively), which was in conflict with the Pauli principle. One quark can carry
 76 one of the three colours (usually called *red*, *green* and *blue*) and antiquark one of
 77 the three anti-colours respectively. Only colour-neutral (or white) particles could
 78 exist. Mesons are assumed to be a colour-anticolour pair, while baryons are *red-*
 79 *green-blue* triplets. Gluons also are colour-charged and there are 8 types of gluons.
 80 Therefore they can interact with themselves [3].

¹The LHCb experiment at CERN in Geneva confirmed recently existence of $Z(4430)$ - a particle consisting of four quarks [2].

81 **1.2.2 Quantum Chromodynamics potential**

82 As a result of that gluons are massless, one can expect, that the static potential
 83 in the QCD will have the similar form like one in the electrodynamics e.g. $\sim 1/r$
 84 (through an analogy to photons). In reality the QCD potential is assumed to have
 85 the form of [3]

$$V_s = -\frac{4}{3} \frac{\alpha_s}{r} + kr, \quad (1.1)$$

86 where the α_s is a coupling constant of the strong force and the kr part is related
 87 with the *confinement*. In comparison to the electromagnetic force, a value of the
 88 strong coupling constant is $\alpha_s \approx 1$ and the electromagnetic one is $\alpha = 1/137$.

89 The fact that quarks does not exist separately, but they are always bound,
 90 is called a confinement. As two quarks are pulled apart, the linear part kr in
 91 the Eq. 1.1 becomes dominant and the potential becomes proportional to the dis-
 92 tance. This situation resembles stretching of a string. At some point, when the
 93 string is so large it is energetically favourable to create a quark-antiquark pair. At
 94 this moment such pair (or pairs) is formed, the string breaks and the confinement
 95 is preserved (Fig. 1.2).

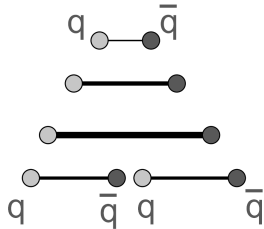


Figure 1.2: A string break and a creation of a pair quark-anti-quark [4].

95 On the other hand, for the small r , an interaction between the quarks and
 96 gluons is dominated by the Coulomb-like term $-\frac{4}{3} \frac{\alpha_s}{r}$. The coupling constant α_s
 97 depends on the four-momentum Q^2 transferred in the interaction. This depend-
 98 ence is presented in Fig. 1.3. The value α_s decreases with increasing momentum
 99 transfer and the interaction becomes weak for large Q^2 , i.e. $\alpha_s(Q) \rightarrow 0$. Be-
 100 cause of weakening of coupling constant, quarks at large energies (or small dis-
 101 tances) are starting to behave like free particles. This phenomenon is known as
 102 an *asymptotic freedom*. The QCD potential has also temperature dependence - the
 103 force strength "melts" with the temperature increase. Therefore the asymptotic
 104 freedom is expected to appear in either the case of high baryon densities (small
 105 distances between quarks) or very high temperatures. This temperature depend-
 106 ence is illustrated in the Fig. 1.4.

107 If the coupling constant α_s is small, one can use perturbative methods to cal-
 108 culate physical observables. Perturbative QCD (pQCD) successfully describes
 109 hard processes (with large Q^2), such as jet production in high energy proton-
 110 antiproton collisions. The applicability of pQCD is defined by the *scale parameter*

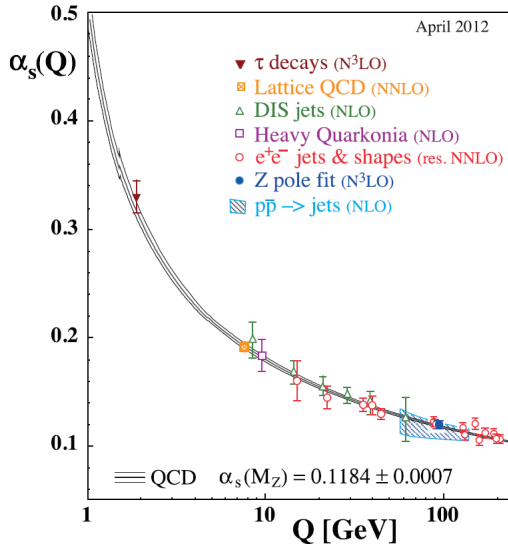


Figure 1.3: The coupling parameter α_s dependence on four-momentum transfer Q^2 [5].

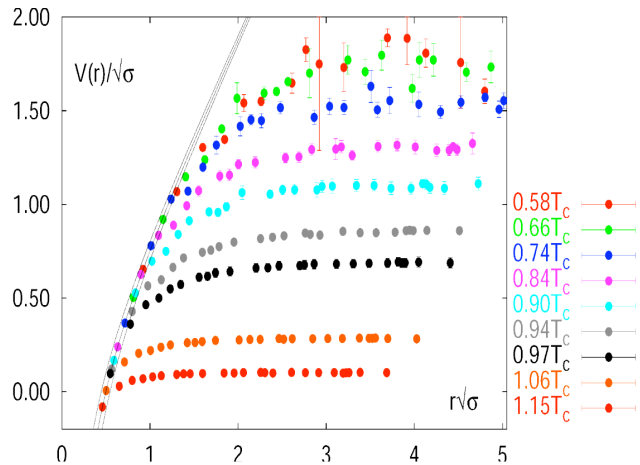


Figure 1.4: The QCD potential for a pair quark-antiquark as a function of distance for different temperatures. A value of a potential decreases with the temperature [4].

112 $\Lambda_{QCD} \approx 200$ MeV. If $Q \gg \Lambda_{QCD}$ then the process is in the perturbative domain
113 and can be described by pQCD. A description of soft processes (when $Q < 1$ GeV)
114 is a problem in QCD - perturbative theory breaks down at this scale. Therefore,
115 to describe processes with low Q^2 , one has to use alternative methods like Lattice
116 QCD. Lattice QCD (LQCD) is non-perturbative implementation of a field theory
117 in which QCD quantities are calculated on a discrete space-time grid. LQCD al-

lows to obtain properties of matter in equilibrium, but there are some limitations. Lattice QCD requires fine lattice spacing to obtain precise results - therefore large computational resources are necessary. With the constant growth of computing power this problem will become less important. The second problem is that lattice simulations are possible only for baryon density $\mu_B = 0$. At $\mu_B \neq 0$, Lattice QCD breaks down because of the sign problem [6].

1.2.3 The quark-gluon plasma

The new state of matter in which quarks are no longer confined is known as a *quark-gluon plasma* (QGP). The predictions coming from the discrete space-time Lattice QCD calculations reveal a phase transition from the hadronic matter to the quark-gluon plasma at the high temperatures and baryon densities. The res-

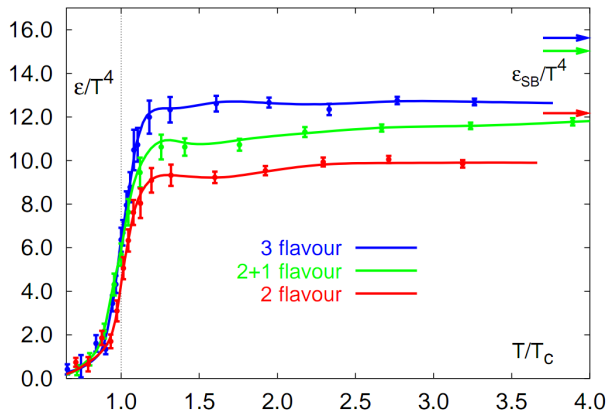


Figure 1.5: A number of degrees of freedom as a function of a temperature [7].

ults obtained from such calculations are shown on Fig. 1.5. The energy density ϵ which is divided by T^4 is a measure of number of degrees of freedom in the system. One can observe significant rise of this value, when the temperature increases past the critical value T_C . Such increase is signaling a phase transition - the formation of QGP [8]. The values of the energy densities plotted in Fig. 1.5 do not reach the Stefan-Boltzmann limit ϵ_{SB} (marked with arrows), which corresponds to an ideal gas. This can indicate some residual interactions in the system. According to the results from the RHIC², the new phase of matter behaves more like an ideal fluid, than like a gas [9].

One of the key questions, to which current heavy ion physics tries to find an answer is the value of a critical temperature T_C as a function of a baryon chemical potential μ_B (baryon density), where the phase transition occur. The results coming from the Lattice QCD are presented in the Fig. 1.6. The phase of matter in which quarks and gluons are deconfined is expected to exist at large

²Relativistic Heavy Ion Collider at Brookhaven National Laboratory in Upton, New York

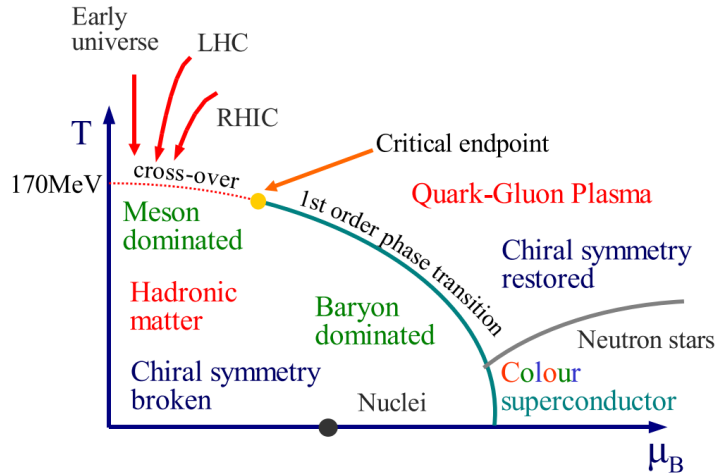


Figure 1.6: Phase diagram coming from the Lattice QCD calculations [8].

temperatures. In the region of small temperatures and high baryon densities, a different state is supposed to appear - a *colour superconductor*. The phase transition between hadronic matter and QGP is thought to be of 1st order at $\mu_B \gg 0$. However as $\mu_B \rightarrow 0$ quarks' masses become significant and a sharp transition transforms into a rapid but smooth cross-over. It is believed that in Pb-Pb collisions observed at the LHC³, the created matter has high enough temperature to be in the quark-gluon plasma phase, then cools down and converts into hadrons, undergoing a smooth transition [8].

1.3 Relativistic heavy ion collisions

1.3.1 Stages of heavy ion collision

To create the quark-gluon plasma one has to achieve high enough temperatures and baryon densities. Such conditions can be recreated in the heavy ion collisions at the high energies. The left side of the Figure 1.7 shows simplified picture of a central collision of two highly relativistic nuclei in the centre-of-mass reference frame. The colliding nuclei are presented as thin disks because of the Lorentz contraction. In the central region, where the energy density is the highest, a new state of matter - the quark-gluon plasma - is supposedly created. Afterwards, the plasma expands ad cools down, quarks combine into hadrons and their mutual interactions cease when the system reaches the *freeze-out* temperature. Subsequently, produced free hadrons move towards the detectors.

On the right side of the Figure 1.7 there is presented a space-time evolution of a collision process, plotted in the light-cone variables (z, t). The two highly

³Large Hadron Collider at CERN, Geneva

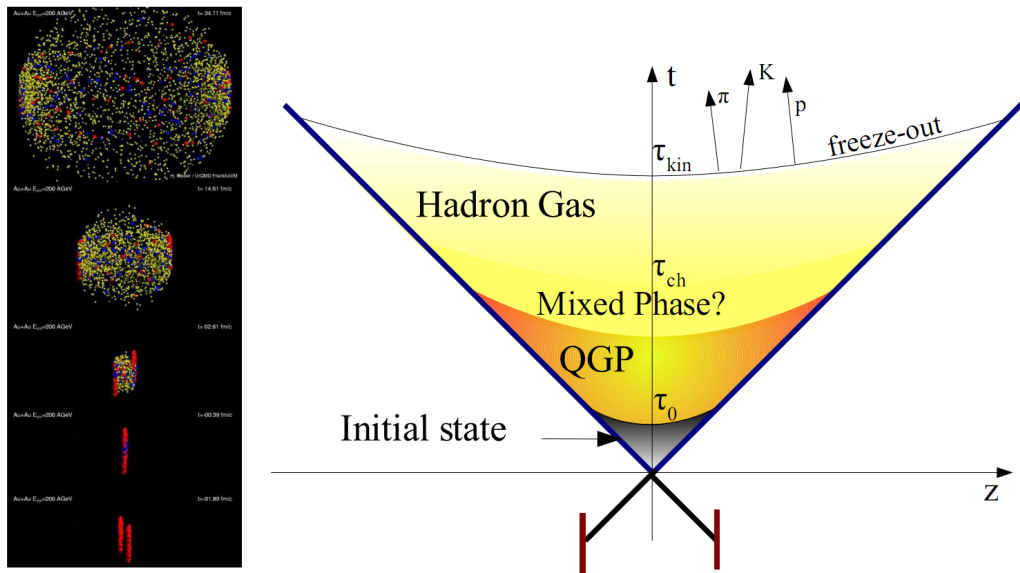


Figure 1.7: Left: stages of a heavy ion collision simulated in the UrQMD model. Right: schematic view of a heavy ion collision evolution [8].

165 relativistic nuclei are traveling basically along the light cone until they collide
 166 at the centre of diagram. Nuclear fragments emerge from the collision again
 167 along the (forward) light cone, while the matter between fragmentation zones
 168 populates the central region. This hot and dense matter is believed to be in the
 169 state of the quark-gluon plasma. There exist several frameworks to describe this
 170 transition to the QGP phase, for example: QCD string breaking, QCD parton cas-
 171 cades or colour glass condensate evolving into glasma and later into quark-gluon
 172 plasma [10].

173 **String breaking** – In the string picture, the nuclei pass through each other forming
 174 colour strings. This is analogous to the situation depicted in the Fig 1.2 - the
 175 colour string is created between quarks inside particular nucleons in nuclei. In
 176 the next step strings decay / fragment forming quarks and gluons or directly
 177 hadrons. This approach becomes invalid at very high energies, when the strings
 178 overlap and cannot be treated as independent objects.

179 **Parton cascade** – The parton⁴ cascade model is based on the pQCD. The col-
 180 liding nuclei are treated as clouds of quarks and which penetrate through each
 181 other. The key element of this method is the time evolution of the parton phase-
 182 space distributions, which is governed by a relativistic Boltzmann equation with
 183 a collision term that contains dominant perturbative QCD interations. The bot-
 184 tleneck of the parton cascade model is the low energies regime, where the Q^2 is
 185 too small to be described by the perturbative theory.

⁴A parton is a common name for a quark and a gluon.

186 **Colour glass condensate** – The colour glass condensate assumes, that the had-
 187 ron can be viewed as a tightly packed system of interacting gluons. The sat-
 188 uration of gluons increases with energy, hence the total number of gluons may
 189 increase without the bound. Such a saturated and weakly coupled gluon system
 190 is called a colour glass condensate. The fast gluons in the condensate are Lorentz
 191 contracted and redistributed on the two very thin sheets representing two col-
 192 liding nuclei. The sheets are perpendicular to the beam axis. The fast gluons
 193 produce mutually orthogonal colour magnetic and electric fields, that only ex-
 194 ist on the sheets. Immediately after the collision, i.e. just after the passage of
 195 the two gluonic sheets after each other, the longitudinal electric and magnetic
 196 fields are produced forming the *glasma*. The glasma fields decay through the
 197 classical rearrangement of the fields into radiation of gluons. Also decays due to
 198 the quantum pair creations are possible. In this way, the quark-gluon plasma is
 199 produced.

200 Interactions within the created quark-gluon plasma bring the system into the
 201 local statistical equilibrium, hence its further evolution can be described by the
 202 relativistic hydrodynamics. The hydrodynamic expansion causes that the sys-
 203 tem becomes more and more dilute. The phase transition from the quark-gluon
 204 plasma to the hadronic gas occurs. Further expansion causes a transition from the
 205 strongly interaction hadronic gas to weakly interacting system of hadrons which
 206 move freely to the detectors. Such decoupling of hadrons is called the *freeze-out*.
 207 The freeze-out can be divided into two phases: the chemical freeze-out and the
 208 thermal one. The *chemical freeze-out* occurs when the inelastic collisions between
 209 constituents of the hadron gas stop. As the system evolves from the chemical
 210 freeze-out to the thermal freeze-out the dominant processes are elastic collisions
 211 (such as, for example $\pi + \pi \rightarrow \rho \rightarrow \pi + \pi$) and strong decays of heavier reso-
 212 nances which populate the yield of stable hadrons. The *thermal freeze-out* is the
 213 stage of the evolution of matter, when the strongly coupled system transforms
 214 to a weakly coupled one (consisting of essentially free particles). In other words
 215 this is the moment, where the hadrons practically stop to interact. Obviously, the
 216 temperatures corresponding to the two freeze-outs satisfy the condition

$$T_{chem} > T_{therm}, \quad (1.2)$$

217 where T_{chem} (inferred from the ratios of hadron multiplicities) is the temperature
 218 of the chemical freeze-out, and T_{therm} (obtained from the investigation of the
 219 transverse-momentum spectra) is the temperature of the thermal freeze-out [10].

220 1.3.2 QGP signatures

221 The quark-gluon plasma is a very short living and unstable state of matter.
 222 One cannot investigate the properties of a plasma and confirm its existence dir-
 223 ectly. Hence, the several experimental effects were proposed as QGP signatures,
 224 some of them have been already observed in heavy ion experiments [8]. As mat-
 225 ter created in the heavy ions collisions is supposed to behave like a fluid, one

should expect appearance of collective behaviour at small transverse momenta - so called *elliptic flow* and *radial flow*. The next signal is the temperature range obtained from the measurements of *direct photons*, which gives us information, that the system created in heavy ion collisions is far above the critical temperature obtained from the LQCD calculations. The *puzzle in the di-lepton spectrum* can be explained by the modification of spectral shape of vector mesons (mostly ρ meson) in the presence of a dense medium. This presence of a medium can also shed light on the *jet quenching* phenomenon - the suppression occurrence in the high p_T domain.

Elliptic flow

In a non-central heavy ion collisions, created region of matter has an almond shape with its shorter axis in the *reaction plane* (Fig. 1.8). The pressure gradient is much larger in-plane rather than out-of-plane. This causes larger acceleration and transverse velocities in-plane rather than out-of-plane. Such differences can

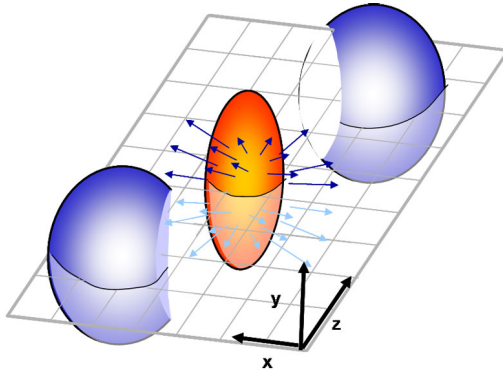


Figure 1.8: Overlapping region which is created in heavy ion collisions has an almond shape. Visible x-z plane is a *reaction plane*. The x-y plane is a *transverse plane*. The z is a direction of the beam [11].

be investigated by studying the distribution of particles with respect to the reaction plane orientation [12]:

$$E \frac{d^3 N}{dp^3} = \frac{1}{2\pi} \frac{d^2 N}{p_T dp_T dy} (1 + 2v_1 \cos(\phi) + 2v_2 \cos(2\phi) + \dots), \quad (1.3)$$

where ϕ is the angle between particle transverse momentum p_T (a momentum projection on a transverse plane) and the reaction plane, N is a number of particles and E is an energy of a particle. The y variable is a *rapidity* defined as:

$$y = \frac{1}{2} \ln \left(\frac{E + p_L}{E - p_L} \right), \quad (1.4)$$

245 where p_L is a longitudinal component of a momentum (parallel to the beam direction).
 246 The v_n coefficients indicate the shape of a system. For the most central collisions
 247 ($b = 0$ - see Fig. 1.9) all coefficients vanish $\sum_{n \in N_+} v_n = 0$ (the overlapping region has the spherical shape). The Fourier series elements in the parentheses

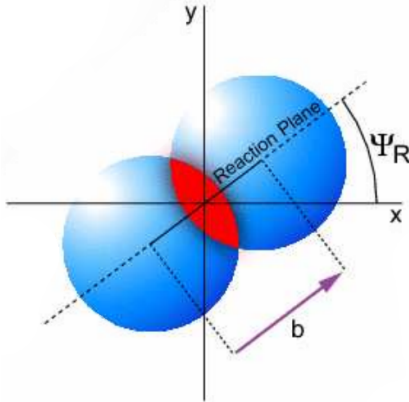


Figure 1.9: Cross-section of a heavy ion collision in a transverse plane. Ψ_R is an angle between transverse plane and the reaction plane. The b parameter is an *impact parameter* - a distance between centers of nuclei during a collision. An impact parameter is related with the centrality of a collision and a volume of the quark-gluon plasma [12].

248 in Eq. 1.3 represent different kinds of a flow. The first value: "1" represents the
 249 *radial flow* - an isotropic flow in every direction. Next coefficient v_1 is responsible
 250 for *direct flow*. The v_2 coefficient is a measure of elliptic anisotropy (*elliptic flow*).
 251 The v_2 has to build up in the early stage of a collision - later the system becomes
 252 too dilute: space asymmetry and the pressure gradient vanish. Therefore the
 253 observation of elliptic flow means that the created matter was in fact a strongly
 254 interacting matter.

255 The v_2 coefficient was measured already at CERN SPS, LHC and RHIC. For
 256 the first time hydrodynamics successfully described the collision dynamics as the
 257 measured v_2 reached hydrodynamic limit (Fig. 1.10). As expected, there is a mass
 258 ordering of v_2 as a function of p_T (lower plot in the Fig. 1.10) with pions having
 259 the largest and protons the smallest anisotropy. In the upper plots in the Fig. 1.10
 260 there is a v_2 as a function of transverse kinetic energy. The left plot shows the
 261 two universal trend lines for baryons and mesons. After the scaling of v_2 and the
 262 kinetic energy by the number of valence quarks, all of the hadrons follow the
 263 same universal curve. Those plots show that strong collectivity is observed in
 264 heavy ion collisions.

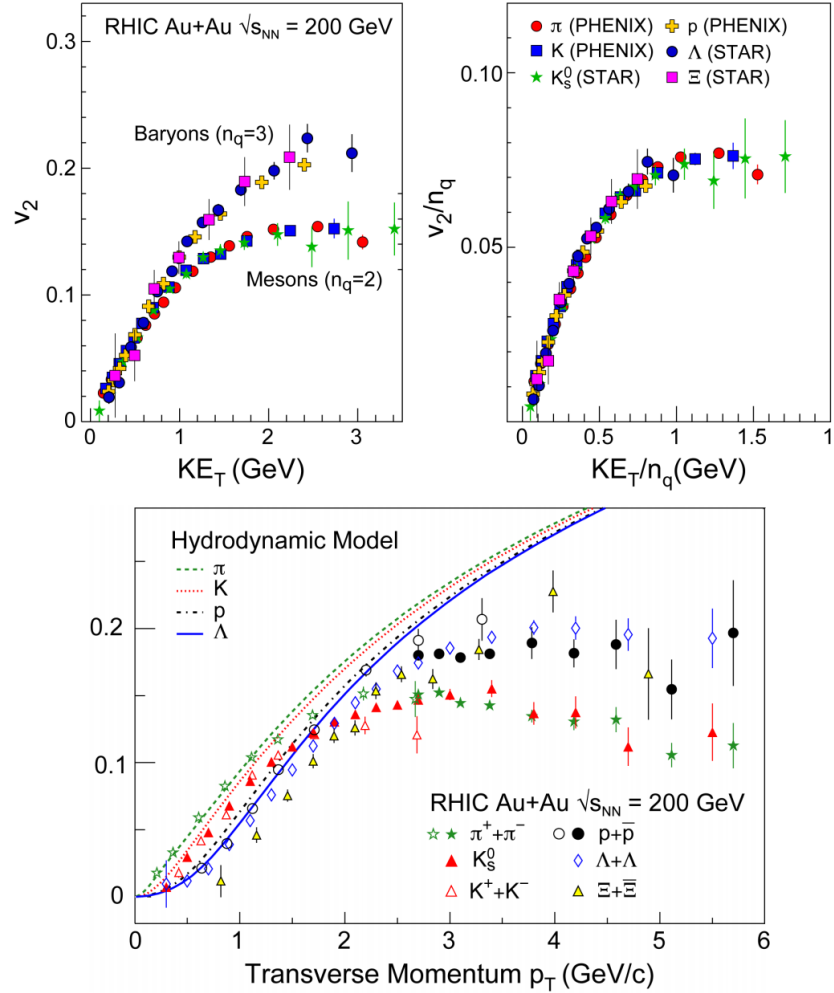


Figure 1.10: *Lower:* The elliptic flow v_2 follows the hydrodynamical predictions for an ideal fluid perfectly. Note that > 99% of all final hadrons have $p_T < 1.5$ GeV/c. *Upper left:* The v_2 plotted versus transverse kinetic energy $KE_T = m_T - m_0 = \sqrt{p_T^2 + m_0^2} - m_0$. The v_2 follows different universal curves for mesons and baryons. *Upper right:* When scaled by the number of valence quarks, the v_2 follows the same universal curve for all hadrons and for all values of scaled transverse kinetic energy [13].

266 Transverse radial flow

267 Elliptic flow described previously is caused by the pressure gradients which
 268 must also produce a more simple collective behaviour of matter - a movement
 269 inside-out, called radial flow. Particles are pushed to higher momenta and they
 270 move away from the center of the collision. A source not showing collective

271 behaviour, like pp collisions, produces particle spectra that can be fitted by a
 272 power-law [8]:

$$\frac{1}{2\pi p_T} \frac{d^2N}{dp_T d\eta} = C \left(1 + \frac{p_T}{p_0} \right)^{-n}. \quad (1.5)$$

273 The η variable is a *pseudorapidity* defined as follows:

$$\eta = \frac{1}{2} \ln \left(\frac{p + p_L}{p - p_L} \right) = -\ln \left(\frac{\theta}{2} \right), \quad (1.6)$$

where θ is an emission angle $\cos \theta = p_L/p$.

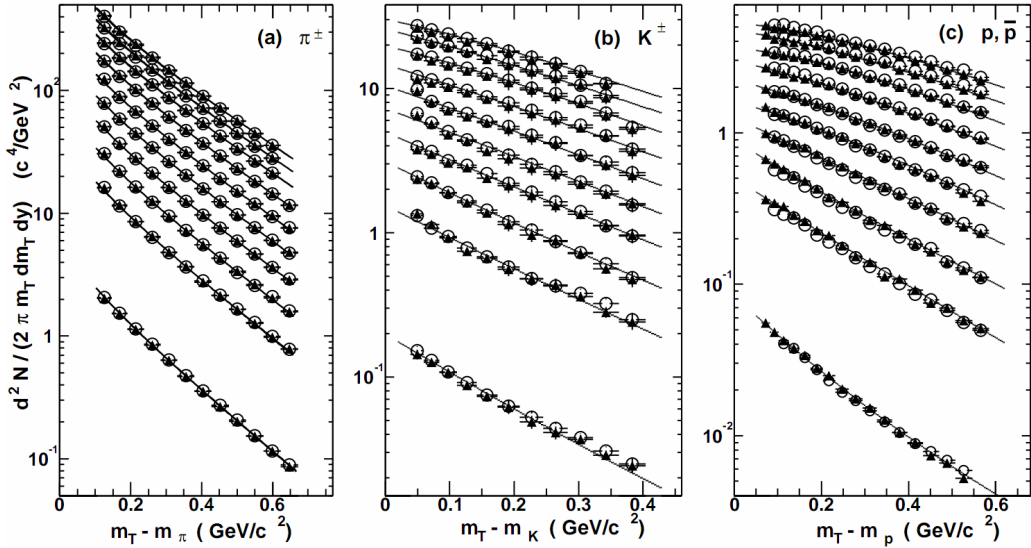


Figure 1.11: Invariant yield of particles versus transverse mass $m_T = \sqrt{p_T^2 + m_0^2}$ for π^\pm , K^\pm , p and \bar{p} at mid-rapidity for p+p collisions (bottom) and Au+Au events from 70-80% (second bottom) to 0-5% (top) centrality [14].

274
 275 The hydrodynamical expansion of a system gives the same flow velocity kick
 276 for different kind of particles - ones with bigger masses will gain larger p_T boost.
 277 This causes increase of the yield of particles with larger transverse momenta. In
 278 the invariant yield plots one can observe the decrease of the slope parameter,
 279 especially for the heavier hadrons. This is presented in the Fig. 1.11. The most
 280 affected spectra are ones of kaons (b) and protons (c). One can notice decrease
 281 of the slope parameter for heavy ion collisions (plots from second bottom to top)
 282 comparing to the proton-proton collisions (bottom ones), where no boost from
 283 radial flow should occur [8].

284 Direct photons

285 The direct photons are photons, which are not coming from the final state
 286 hadrons decays. Their sources can be various interaction from charged particles

created in the collision, either at the partonic or at the hadronic level. Direct photons are considered to be an excellent probe of the early stage of the collision. This is because their mean free path is very large to the created system in the collision. Thus photons created at the early stage leave the system without suffering any interaction and retain information about this stage, in particular about its temperature.

One can distinguish two kinds of direct photons: *thermal* and *prompt*. Thermal photons can be emitted from the strong processes in the quark-gluon plasma involving quarks and gluons or hot hadronic matter (e.g. processes: $\pi\pi \rightarrow \rho\gamma$, $\pi\rho \rightarrow \pi\gamma$). Thermal photons can be observed in the low p_T region. Prompt photons are believed to come from “hard” collisions of initial state partons belonging to the colliding nuclei. The prompt photons can be described using the pQCD. They will dominate the high p_T region. The analysis of transverse momentum of spectra of direct photons revealed, that the temperature of the source of thermal photons produced in heavy ion collisions at RHIC is in the range 300–600 MeV (Fig. 1.12). Hence the direct photons had to come from a system whose temperature is far above from the critical temperature for QGP creation.

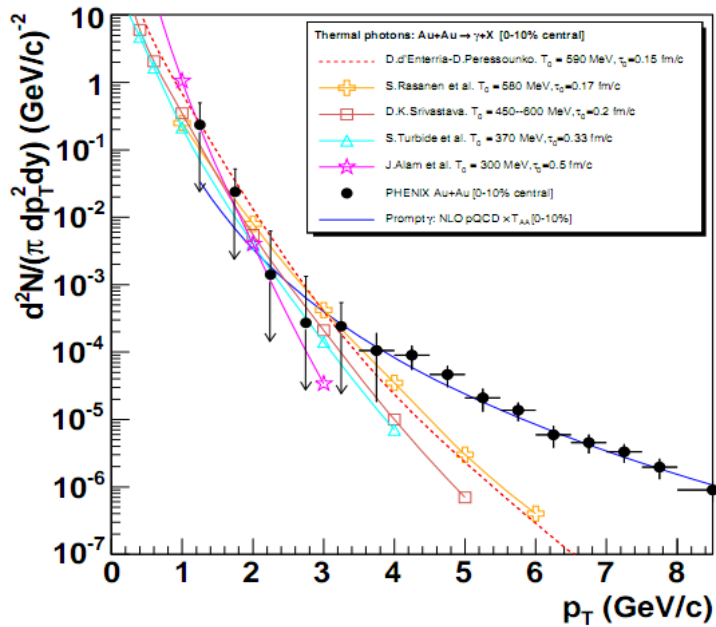


Figure 1.12: Thermal photons spectra for the central Au+Au collisions at $\sqrt{s_{NN}} = 200$ GeV computed within different hydrodynamical models compared with the pQCD calculations (solid line) and experimental data from PHENIX (black dots) [15].

304 **Puzzle in di-lepton mass spectrum**

305 The invariant mass spectra (Fig. 1.13) of lepton pairs reveal many peaks cor-
 306 responding to direct decays of various mesons into a lepton pair. The continu-
 307 ous background in this plot is caused by the decays of hadrons into more than
 308 two leptons (including so-called *Dalitz decays* into a lepton pair and a photon).
 Particular hadron decay channels, which contribute to this spectrum are shown

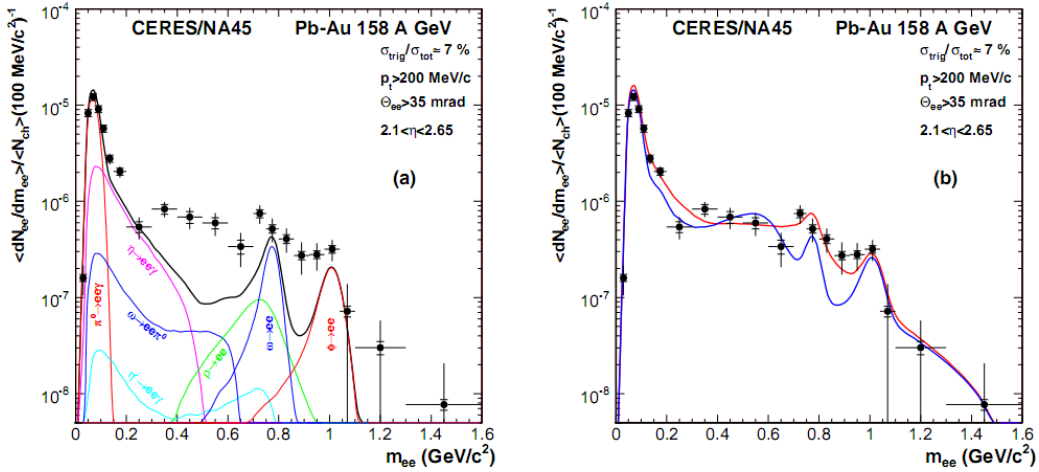


Figure 1.13: Left: Invariant mass spectrum of $e^+ - e^-$ pairs in $\text{Pb} + \text{Au}$ collisions at 158A GeV compared to the sum coming from the hadron decays predictions. Right: The expectations coming from model calculations assuming a dropping of the ρ mass (blue) or a spread of the ρ width in the medium (red) [16].

309
 310 in the Fig. 1.13 with the coloured lines and their sum with the black one. The
 311 sum (called *the hadronic cocktail*) of various components describes experimen-
 312 tal spectra coming from the simple collisions (like $p + p$ or $p + A$) quite well with the
 313 statistical and systematical uncertainties [9]. This situation is different consider-
 314 ing more complicated systems i.e. $A + A$. Spectra coming from $\text{Pb} + \text{Au}$ collisions
 315 are presented on the plots in the Fig. 1.13. The “hadronic cocktail” does not de-
 316 scribe the data, in the mass range between the π and the ρ mesons a significant
 317 excess of electron pairs over the calculated sum is observed. Theoretical expla-
 318 nation of this phenomenon assumes modification of the spectral shape of vector
 319 mesons in a dense medium. Two different interpretations of this increase were
 320 proposed: a decrease of meson mass with the medium density and increase of the
 321 meson width in the dense medium. In principle, one could think of simultaneous
 322 occurrence of both effects: mass shift and resonance broadening. Experimental
 323 results coming from the CERES disfavour the mass shift hypothesis indicating
 324 only broadening of resonance peaks (Fig. 1.13b) [9].

325 **Jet quenching**

326 A jet is defined as a group of particles with close vector momenta and high en-
 327 ergies. It has its beginning when the two partons are going in opposite directions
 328 and have energy big enough to produce new quark-antiquark pair and then ra-
 329 diate gluons. This process can be repeated many times and it results in two back-
 330 to-back jets of hadrons. It has been found that jets in the opposite hemisphere
 331 (*away-side jets*) show a very different pattern in d+Au and Au+Au collisions. This
 332 is shown in the azimuthal correlations in the Fig. 1.14. In d+Au collisions, like in
 333 p+p, a pronounced away-side jet appears around $\Delta\phi = \pi$, exactly opposite to the
 334 trigger jet, what is typical for di-jet events. In central Au+Au collisions the away-
 jet is suppressed. When the jet has its beginning near the surface of the quark-

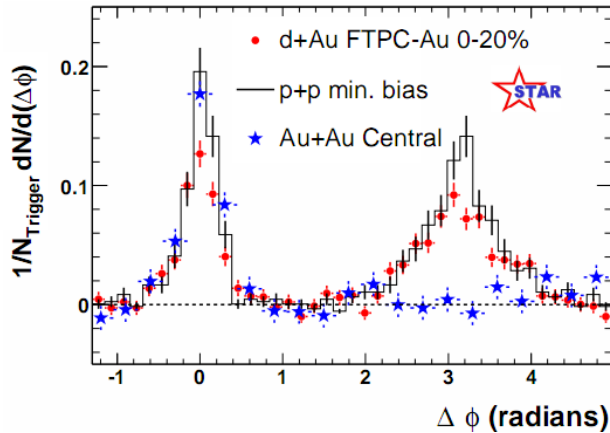


Figure 1.14: Azimuthal angle difference $\Delta\phi$ distributions for different colliding systems at $\sqrt{s_{NN}} = 200$ GeV. Transverse momentum cut: $p_T > 2$ GeV. For the Au+Au collisions the away-side jet is missing [17].

335 gluon plasma, one of the jets (*near-side jet*) leaves the system almost without any
 336 interactions. This jet is visible on the correlation plot as a high peak at $\Delta\phi = 0$.
 337 However, the jet moving towards the opposite direction has to penetrate a dense
 338 medium. The interaction with the plasma causes energy dissipation of particles
 339 and is visible on an azimuthal correlation plot as disappearance of the away-side
 340 jet [9].

342 **Chapter 2**

343 **Therminator model**

344 THERMINATOR [18] is a Monte Carlo event generator designed to investigate
345 the particle production in the relativistic heavy ion collisions. The functionality
346 of the code includes a generation of the stable particles and unstable resonances
347 at the chosen hypersurface model. It performs the statistical hadronization which
348 is followed by space-time evolution of particles and the decay of resonances. The
349 key element of this method is an inclusion of a complete list of hadronic reso-
350 nances, which contribute very significantly to the observables. The second version
351 of THERMINATOR [19] comes with a possibility to incorporate any shape of freeze-
352 out hypersurface and the expansion velocity field, especially those generated ex-
353 ternally with various hydrodynamic codes.

354 **2.1 (3+1)-dimensional viscous hydrodynamics**

355 Most of the relativistic viscous hydrodynamic calculations are done in
356 (2+1)-dimensions. Such simplification assumes boost-invariance of a matter
357 created in a collision. Experimental data reveals that no boost-invariant region is
358 formed in the collisions [20]. Hence, for the better description of created system
359 a (3+1)-dimensional model is required.

360 In the four dimensional relativistic dynamics one can describe a system
361 using a space-time four-vector $x^\nu = (ct, x, y, z)$, a velocity four-vector
362 $u^\nu = \gamma(c, v_x, v_y, v_z)$ and a energy-momentum tensor $T^{\mu\nu}$. The particular
363 components of $T^{\mu\nu}$ have a following meaning:

- 364 • T^{00} - an energy density,
- 365 • $cT^{0\alpha}$ - an energy flux across a surface x^α ,
- 366 • $T^{\alpha 0}$ - an α -momentum flux across a surface x^α multiplied by c ,
- 367 • $T^{\alpha\beta}$ - components of momentum flux density tensor,

368 where $\gamma = (1 - v^2/c^2)^{-1/2}$ is Lorentz factor and $\alpha, \beta \in \{1, 2, 3\}$. Using u^ν one can
 369 express $T^{\mu\nu}$ as follows [21]:

$$T_0^{\mu\nu} = (e + p)u^\mu u^\nu - pg^{\mu\nu} \quad (2.1)$$

370 where e is an energy density, p is a pressure and $g^{\mu\nu}$ is an inverse metric tensor:

$$g^{\mu\nu} = \begin{bmatrix} 1 & 0 & 0 & 0 \\ 0 & -1 & 0 & 0 \\ 0 & 0 & -1 & 0 \\ 0 & 0 & 0 & -1 \end{bmatrix}. \quad (2.2)$$

371 The presented version of energy-momentum tensor (Eq. 2.1) can be used to de-
 372 scribe dynamics of a perfect fluid. To take into account influence of viscosity,
 373 one has to apply the following corrections coming from shear $\pi^{\mu\nu}$ and bulk Π
 374 viscosities [22]:

$$T^{\mu\nu} = T_0^{\mu\nu} + \pi^{\mu\nu} + \Pi(g^{\mu\nu} - u^\mu u^\nu). \quad (2.3)$$

375 The stress tensor $\pi^{\mu\nu}$ and the bulk viscosity Π are solutions of dynamical equa-
 376 tions in the second order viscous hydrodynamic framework [21]. The compari-
 377 son of hydrodynamics calculations with the experimental results reveal, that the
 378 shear viscosity divided by entropy η/s has to be small and close to the AdS/CFT
 379 estimate $\eta/s = 0.08$ [22, 23]. The bulk viscosity over entropy value used in calcu-
 380 lations is $\zeta/s = 0.04$ [22].

381 When using $T^{\mu\nu}$ to describe system evolving close to local thermodynamic
 382 equilibrium, relativistic hydrodynamic equations in a form of:

$$\partial_\mu T^{\mu\nu} = 0 \quad (2.4)$$

383 can be used to describe the dynamics of the local energy density, pressure and
 384 flow velocity.

385 Hydrodynamic calculations are starting from the Glauber¹ model initial con-
 386 ditions. The collective expansion of a fluid ends at the freeze-out hypersurface.
 387 That surface is usually defined as a constant temperature surface, or equivalently
 388 as a cut-off in local energy density. The freeze-out is assumed to occur at the
 389 temperature $T = 140$ MeV.

390 2.2 Statistical hadronization

391 Statistical description of heavy ion collision has been successfully used
 392 to describe quantitatively *soft* physics, i.e. the regime with the transverse
 393 momentum not exceeding 2 GeV. The basic assumption of the statistical
 394 approach of evolution of the quark-gluon plasma is that at some point of the

¹The Glauber Model is used to calculate “geometrical” parameters of a collision like an impact parameter, number of participating nucleons or number of binary collisions.

395 space-time evolution of the fireball, the thermal equilibrium is reached. When
 396 the system is in the thermal equilibrium the local phase-space densities of
 397 particles follow the Fermi-Dirac or Bose-Einstein statistical distributions. At
 398 the end of the plasma expansion, the freeze-out occurs. The freeze-out model
 399 incorporated in the THERMINATOR model assumes, that chemical and thermal
 400 freeze-out occur at the same time.

401 **2.2.1 Cooper-Frye formalism**

402 The result of the hydrodynamic calculations is the freeze-out hyper-
 403 surface Σ^μ . A three-dimensional element of the surface is defined as [19]

$$404 \quad d\Sigma_\mu = \epsilon_{\mu\alpha\beta\gamma} \frac{\partial x^\alpha}{\partial \alpha} \frac{\partial x^\beta}{\partial \beta} \frac{\partial x^\gamma}{\partial \gamma} d\alpha d\beta d\gamma, \quad (2.5)$$

405 where $\epsilon_{\mu\alpha\beta\gamma}$ is the Levi-Civita tensor and the variables $\alpha, \beta, \gamma \in \{1, 2, 3\}$ are used
 406 to parametrize the three-dimensional freeze-out hypersurface in the Minkowski
 407 four-dimensional space. The Levi-Civita tensor is equal to 1 when the indices
 408 form an even permutation (eg. ϵ_{0123}), to -1 when the permutation is odd (e.g.
 409 ϵ_{2134}) and has a value of 0 if any index is repeated. Therefore [19],

$$410 \quad d\Sigma_0 = \begin{vmatrix} \frac{\partial x}{\partial \alpha} & \frac{\partial x}{\partial \beta} & \frac{\partial x}{\partial \gamma} \\ \frac{\partial y}{\partial \alpha} & \frac{\partial y}{\partial \beta} & \frac{\partial y}{\partial \gamma} \\ \frac{\partial z}{\partial \alpha} & \frac{\partial z}{\partial \beta} & \frac{\partial z}{\partial \gamma} \end{vmatrix} d\alpha d\beta d\gamma \quad (2.6)$$

411 and the remaining components are obtained by cyclic permutations of t, x, y
 412 and z .

413 One can obtain the number of hadrons produced on the hypersurface Σ^μ from
 414 the Cooper-Frye formalism. The following integral yields the total number of
 415 created particles [19]:

$$416 \quad N = (2s + 1) \int \frac{d^3 p}{(2\pi)^3 E_p} \int d\Sigma_\mu p^\mu f(p_\mu u^\mu), \quad (2.7)$$

417 where $f(p_\mu u^\mu)$ is the phase-space distribution of particles (for stable ones and res-
 418 onances). One can simply derive from Eq. 2.7, the dependence of the momentum
 419 density [24]:

$$420 \quad E \frac{d^3 N}{dp^3} = \int d\Sigma_\mu f(p_\mu u^\mu) p^\mu. \quad (2.8)$$

421 The momentum distribution f contains non-equilibrium corrections:

$$422 \quad f = f_0 + \delta f_{shear} + \delta f_{bulk}, \quad (2.9)$$

423 where

$$424 \quad f_0(p_\mu u^\mu) = \left\{ \exp \left[\frac{p_\mu u^\mu - (B\mu_B + I_3\mu_{I_3} + S\mu_S + C\mu_C)}{T} \right] \pm 1 \right\}^{-1} \quad (2.10)$$

420 In case of fermions, in the Eq. 2.10 there is a plus sign and for bosons, minus
 421 sign respectively. The thermodynamic quantities appearing in the $f_0(\cdot)$ are T -
 422 temperature, μ_B - baryon chemical potential, μ_{I_3} - isospin chemical potential, μ_S
 423 - strange chemical potential, μ_C - charmed chemical potential and the s is a spin of
 424 a particle. The hydrodynamic calculations yield the flow velocity at freeze-out as
 425 well as the stress and bulk viscosity tensors required to calculate non-equilibrium
 426 corrections to the momentum distribution used in Eq. 2.7. The term coming from
 427 shear viscosity has a form [22]

$$\delta f_{shear} = f_0(1 \pm f_0) \frac{1}{2T^2(e + p)} p^\mu p^\nu \pi_{\mu\nu} \quad (2.11)$$

428 and bulk viscosity

$$\delta f_{bulk} = C f_0(1 \pm f_0) \left(\frac{(u^\mu p_\mu)^2}{3u^\mu p_\mu} - c_s^2 u^\mu p_\mu \right) \Pi \quad (2.12)$$

429 where c_s is sound velocity and

$$\frac{1}{C} = \frac{1}{3} \frac{1}{(2\pi)^3} \sum_{hadrons} \int d^3 p \frac{m^2}{E} f_0(1 \pm f_0) \left(\frac{p^2}{3E} - c_s^2 E \right). \quad (2.13)$$

430 The equations presented above are directly used in the THERMINATOR to gen-
 431 erate the primordial hadrons (created during freeze-out) with the Monte-Carlo
 432 method. Resonances produced in this way, propagate and decay, in cascades if
 433 necessary. For every generated particle, its origin point either on a hypersurface
 434 or is associated with the point of the decay of the parent particle. This informa-
 435 tion is kept in the simulation due to its importance for the femtoscopic analysis.

⁴³⁶ **Chapter 3**

⁴³⁷ **Particle interferometry**

⁴³⁸ Two-particle interferometry (also called *femtoscopy*) gives a possibility to
⁴³⁹ investigate space-time characteristics of the particle-emitting source created
⁴⁴⁰ in heavy ion collisions. Through the study of particle correlations, their
⁴⁴¹ momentum distributions can be used to obtain information about the spatial
⁴⁴² extent of the created system. Using this method, one can measure sizes of the
⁴⁴³ order of 10^{-15} m and time of the order of 10^{-23} s.

⁴⁴⁴ **3.1 HBT interferometry**

⁴⁴⁵ In the 1956 Robert Hanbury Brown and Richard Q. Twiss proposed a
⁴⁴⁶ method which through analysis of interference between photons allowed to
⁴⁴⁷ investigate angular dimensions of stars. The most important result from the
⁴⁴⁸ Hanbury-Brown-Twiss experiments is that two indistinguishable particles can
⁴⁴⁹ produce an interference effect. There is almost no difference between normal
⁴⁵⁰ interferometry and HBT method, except that the latter one does not take into
⁴⁵¹ account information about phase shift of registered particles. At the beginning
⁴⁵² this method was used in astronomy for photon interference, but this effect can
⁴⁵³ be used also to measure extent of any emitting source. This method was adapted
⁴⁵⁴ to heavy ion collisions to investigate dimensions of a system created in those
⁴⁵⁵ collisions by studying correlations of identical particles [25]. The main difference
⁴⁵⁶ between HBT method in astronomy and femtoscopy is that the first one is based
⁴⁵⁷ on space-time HBT correlations and the latter one uses momentum correlations.
⁴⁵⁸ The momentum correlations yield the space-time picture of the source, whereas
⁴⁵⁹ the space-time HBT correlations provide the characteristic relative momenta of
⁴⁶⁰ emitted photons, which gives the angular size of the star without the knowledge
⁴⁶¹ of its radius and lifetime [10].

462 3.2 Theoretical approach

463 Intensity interferometry in heavy ion physics uses similar mathematical form-
 464 alism as the astronomy HBT measurement. Through the measurement of corre-
 465 lation between particles as a function of their relative momentum one can deduce
 466 the average separation between emitting sources.

467 **3.2.1 Conventions used**

468 In heavy ion collisions to describe particular directions, components of mo-
 469 mentum and location of particles, one uses naming convention called the Bertsch-
 Pratt coordinate system. This system is presented in the Fig. 3.1. The three dir-

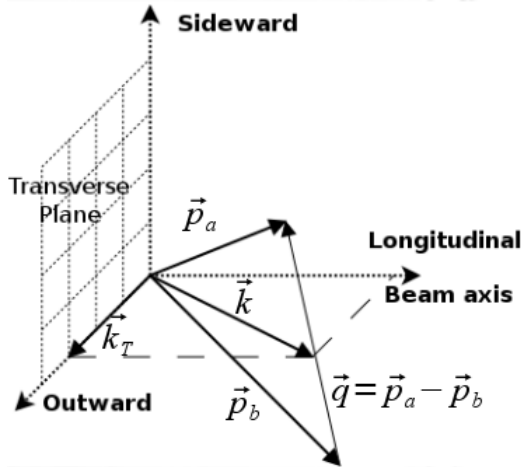


Figure 3.1: Bertsch-Pratt direction naming convention used in heavy ion collision.

470 ections are called *longitudinal*, *outward* and *sideward*. The longitudinal direction
 471 is parallel to the beam axis. The plane perpendicular to the beam axis is called
 472 a *transverse plane*. A projection of a particle pair momentum $\mathbf{k} = (\mathbf{p}_a + \mathbf{p}_b)/2$
 473 on a transverse plane (a *transverse momentum* \mathbf{k}_T) determines *outward* direction:
 474 $(\mathbf{k})_{out} = \mathbf{k}_T$. A direction perpendicular to the longitudinal and outward is called
 475 *sideward*.

476 A particle pair is usually described using two coordinate systems. The first
 477 one, *Longitudinally Co-Moving System* (**LCMS**) is moving along the particle pair
 478 with the longitudinal direction, in other words, the pair longitudinal momentum
 479 vanishes: $(\mathbf{p}_a)_{long} = -(\mathbf{p}_b)_{long}$. The second system is called *Pair Rest Frame* (**PRF**).
 480 In the PRF the centre of mass rests: $\mathbf{p}_a = -\mathbf{p}_b$. Variables which are expressed in
 481 the PRF are marked with a star (e.g. \mathbf{k}^*).

482 The transition of space-time coordinates from LCMS to PRF is simply
 a boost along the outward direction, with the transverse velocity of the

pair $\beta_T = (\mathbf{v}/c)_{out}$ [25]:

$$r_{out}^* = \gamma_t(r_{out} - \beta_T \Delta t) \quad (3.1)$$

$$r_{side}^* = r_{side} \quad (3.2)$$

$$r_{long}^* = r_{long} \quad (3.3)$$

$$\Delta t^* = \gamma_T(\Delta t - \beta_T r_{out}) , \quad (3.4)$$

where $\gamma_T = (1 - \beta_T^2)^{-1/2}$ is the Lorentz factor. However, in calculations performed in this work the equal time approximation is used, which assumes that particles in a pair were produced at the same time in PRF - the Δt^* is neglected.

The most important variables used to describe particle pair are their total momentum $\mathbf{P} = \mathbf{p}_a + \mathbf{p}_b$ and relative momentum $\mathbf{q} = \mathbf{p}_a - \mathbf{p}_b$. In the PRF one has $\mathbf{q} = 2\mathbf{k}^*$, where \mathbf{k}^* is a momentum of the first particle in PRF.

3.2.2 Two particle wave function

Let us consider two identical particles with momenta \mathbf{p}_1 and \mathbf{p}_2 emitted from space points \mathbf{x}_1 and \mathbf{x}_2 . Those emitted particles can be treated as two incoherent waves. If the particles are identical, they are also indistinguishable, therefore one

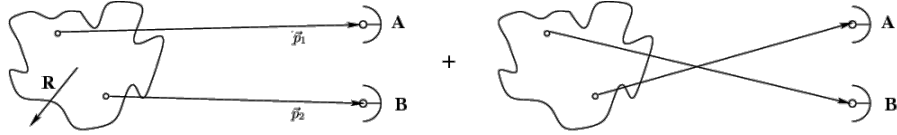


Figure 3.2: The pair wave function is a superposition of all possible states. In case of particle interferometry it includes two cases: particles with momenta p_1, p_2 registered by detectors A, B and p_1, p_2 registered by B, A respectively.

has also take into account the scenario, where the particle with momentum \mathbf{p}_1 is emitted from \mathbf{x}_2 and particle \mathbf{p}_2 from \mathbf{x}_1 (Fig. 3.2). In such case, the wave function describing behaviour of a pair has to contain both components [8]:

$$\Psi_{ab}(\mathbf{q}) = \frac{1}{\sqrt{2}} [\exp(-i\mathbf{p}_1\mathbf{x}_1 - i\mathbf{p}_2\mathbf{x}_2) \pm \exp(-i\mathbf{p}_2\mathbf{x}_1 - i\mathbf{p}_1\mathbf{x}_2)] . \quad (3.5)$$

A two particle wave function of identical bosons is symmetric ("+" sign in Eq. 3.5) and in case of identical fermions - antisymmetric ("−" sign). This anti-symmetrization or symmetrization implies the correlation effect coming from the Fermi-Dirac or Bose-Einstein statistics accordingly.

To provide full description of a system consisting of two charged hadrons, one has to include in the wave function besides quantum statistics also Coulomb and strong Final State Interactions. Considering identical particles systems, the quantum statistics is a main source of a correlation. Hence, in case of space-time analysis of particle emitting source, effects coming from the Coulomb and Strong interactions can be neglected.

506 **3.2.3 Source emission function**

507 To describe particle emitting source, one uses a single emission function [25]:

508

$$S_A(\mathbf{x}_1, \mathbf{p}_1) = \int S(\mathbf{x}_1, \mathbf{p}_1, \mathbf{x}_2, \mathbf{p}_2, \dots, \mathbf{x}_N, \mathbf{p}_N) d\mathbf{x}_2 d\mathbf{p}_2 \dots d\mathbf{x}_N d\mathbf{p}_N \quad (3.6)$$

509 and a two-particle one:

$$S_{AB}(\mathbf{x}_1, \mathbf{p}_1, \mathbf{x}_2, \mathbf{p}_2) = \int S(\mathbf{x}_1, \mathbf{p}_1, \mathbf{x}_2, \mathbf{p}_2, \dots, \mathbf{x}_N, \mathbf{p}_N) d\mathbf{x}_3 d\mathbf{p}_3 \dots d\mathbf{x}_N d\mathbf{p}_N . \quad (3.7)$$

510 Emission function $S(\cdot)$ can be interpreted as a probability to emit a particle, or
 511 a pair of particles from a given space-time point with a given momentum. In
 512 principle, the source emission function should encode all physics aspects of the
 513 particle emission process i.e. the symmetrization for bosons and fermions, as
 514 well as the two-body and many body Final State Interactions. Instead of this,
 515 one assume that each particle's emission process is independent - the interac-
 516 tion between final-state particles after their creation is independent from their
 517 emission process. The assumption of this independence allows to construct two-
 518 particle emission function from single particle emission functions via a convolu-
 519 tion [25]:

$$S(\mathbf{k}^*, \mathbf{r}^*) = \int S_A(\mathbf{p}_1, \mathbf{x}_1) S_B(\mathbf{p}_2, \mathbf{x}_2) \delta \left[\mathbf{k}^* - \frac{\mathbf{p}_1 + \mathbf{p}_2}{2} \right] \delta [\mathbf{r}^* - (\mathbf{x}_1 + \mathbf{x}_2)] \times d^4 \mathbf{x}_1 d^4 \mathbf{x}_2 d^4 \mathbf{x}_1 d^3 \mathbf{p}_1 d^3 \mathbf{p}_2 \quad (3.8)$$

520 In case of identical particles, ($S_A = S_B$) several simplifications can be made.
 521 A convolution of the two same Gaussian distributions is also a Gaussian distri-
 522 bution with σ multiplied by $\sqrt{2}$. Femtoscopy can give information only about
 523 two-particle emission function, but when considering Gaussian distribution as
 524 a source function in Eq. 3.8, one can obtain a σ of a single emission function
 525 from a two-particle emission function. The Eq. 3.8 is not reversible - an inform-
 526 ation about $S_A(\cdot)$ cannot be derived from $S_{AB}(\cdot)$. An exception from this rule
 527 is a Gaussian source function, hence it is often used in femtoscopic calculations.
 528 Considering pairs of identical particles, an emission function is assumed to be
 529 described by the following equation in the Pair Rest Frame [25]:

$$S_{1D}^{PRF}(\mathbf{r}^*) = \exp \left(-\frac{r_{out}^{*2} + r_{side}^{*2} + r_{long}^{*2}}{4R_{inv}^2} \right) . \quad (3.9)$$

To change from the three-dimensional variables to the one-dimensional variable
 one requires introduction of the proper Jacobian r^{*2} .

$$S_{1D}^{PRF}(r^*) = r^{*2} \exp \left(-\frac{r^{*2}}{4R_{inv}^2} \right) . \quad (3.10)$$

530 The “4” in the denominator before the “standard deviation” R_{inv} in the Gaussian
 531 distribution comes from the convolution of the two Gaussian distributions,
 532 which multiplies the R_{inv} by a factor of $\sqrt{2}$.

A more complex form of emission function was used by all RHIC and SPS experiments in identical pion femtoscopy:

$$S_{3D}^{LCMS}(\mathbf{r}) = \exp \left(-\frac{r_{out}^2}{4R_{out}^2} - \frac{r_{side}^2}{4R_{side}^2} - \frac{r_{long}^2}{4R_{long}^2} \right). \quad (3.11)$$

533 The main difference of this source function is that it has three different and inde-
 534 pendent widths R_{out} , R_{side} , R_{long} and they are defined in the LCMS, not in PRF.
 535 Unlike in PRF, in LCMS an equal-time approximation is not used. For identical
 536 particles this is not a problem - only Coulomb interaction inside a wave function
 537 depends on Δt .

538 Relationship between one-dimensional and three-dimensional source sizes

539 Up to now, most of femtoscopic measurements were limited only to averaged
 540 source size R_{av}^L (the letter “L” in superscript stands for LCMS):

$$S_{1D}^{LCMS}(\mathbf{r}) = \exp \left(-\frac{r_{out}^2 + r_{side}^2 + r_{long}^2}{2R_{av}^L} \right). \quad (3.12)$$

541 The relationship between between $S_{1D}^{LCMS}(\cdot)$ and $S_{3D}^{LCMS}(\cdot)$ is given by:

$$S_{3D}^{LCMS}(r) = \int \exp \left(-\frac{r_{out}^2}{2R_{out}^L} - \frac{r_{side}^2}{2R_{side}^L} - \frac{r_{long}^2}{2R_{long}^L} \right) \times \delta \left(r - \sqrt{r_{out}^2 + r_{side}^2 + r_{long}^2} \right) dr_{out} dr_{side} dr_{long}. \quad (3.13)$$

542 The one-dimensional source size corresponding to the three-dimensional one can
 543 be approximated by the following form:

$$S_{1D}^{LCMS}(r) = r^2 \exp \left(-\frac{r^2}{2R_{av}^L} \right). \quad (3.14)$$

544 The equation above assumes that $R_{out}^L = R_{side}^L = R_{long}^L$ hence $R_{av}^L = R_{out}^L$. If this
 545 condition is not satisfied, one can not give explicit mathematical relation between
 546 one-dimensional and three-dimensional source sizes. However, for realistic val-
 547 ues of R (i.e. for similar values of R_{out} , R_{side} , R_{long}), the S_{3D}^{LCMS} from Eq. 3.13 is
 548 not very different from Gaussian distribution and can be well approximated by
 549 Eq. 3.13.

550 A deformation of an averaged source function in case of big differences in
 551 R_{out} , R_{side} , R_{long} is presented in the Fig. 3.3. A three-dimensional Gaussian dis-
 552 tribution with varying widths was averaged into one-dimensional function using

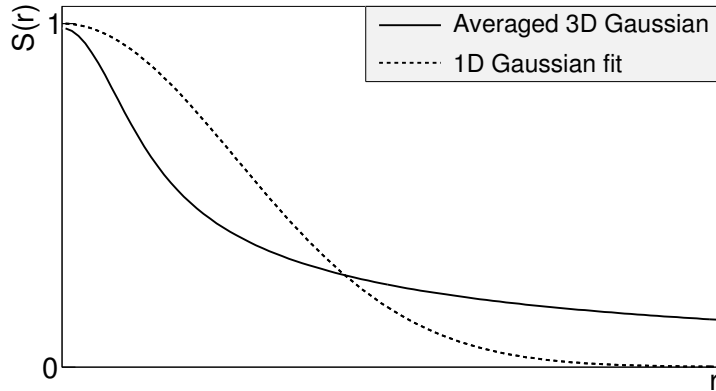


Figure 3.3: An averaged three-dimensional Gaussian source function with different widths was averaged into one-dimensional function. To illustrate deformations, one-dimensional Gaussian distribution was fitted.

the Eq. 3.13. Afterwards, an one-dimensional Gaussian distribution was fitted.
One can notice a heavy tail of an averaged distribution in long r region, which
makes an approximation using one-dimensional distribution in this case quite
inaccurate.

Using Eq. 3.13 and Eq. 3.14 one can obtain a relation between one-dimensional width and the three-dimensional ones. Through numerical calculations one can find the following approximate relation [25]:

$$R_{av}^L = \sqrt{\left(R_{out}^{L^2} + R_{side}^{L^2} + R_{long}^{L^2}\right)/3}. \quad (3.15)$$

This equation does not depend on the pair velocity, hence it is valid in the LCMS and PRF.

3.2.4 Theoretical correlation function

The fundamental object in a particle interferometry is a correlation function. The correlation function is defined as:

$$C(\mathbf{p}_a, \mathbf{p}_b) = \frac{P_2(\mathbf{p}_a, \mathbf{p}_b)}{P_1(\mathbf{p}_a)P_1(\mathbf{p}_b)}, \quad (3.16)$$

where P_2 is a conditional probability to observe a particle with momentum \mathbf{p}_b if particle with momentum \mathbf{p}_a was also observed. A P_1 is a probability to observe a particle with a given momentum. The relationship between source emission function, pair wave function and the correlation function is described by the following equation:

$$C(\mathbf{p}_1, \mathbf{p}_2) = \int S_{AB}(\mathbf{p}_1, \mathbf{x}_1, \mathbf{p}_2, \mathbf{x}_2) |\Psi_{AB}|^2 d^4\mathbf{x}_1 d^4\mathbf{x}_2 \quad (3.17)$$

Substituting the one-dimensional emission function (Eq. 3.10) into the integral above yields the following form of correlation function in PRF:

$$C(q) = 1 + \lambda \exp(-R_{inv}^2 q^2) \quad (3.18)$$

where q is a momentum difference between two particles. When using the three-dimensional emission function (Eq. 3.11) one gets the following correlation function defined in the LCMS:

$$C(\mathbf{q}) = 1 + \lambda \exp(-R_{out}^2 q_{out}^2 - R_{side}^2 q_{side}^2 - R_{long}^2 q_{long}^2) \quad (3.19)$$

567 where q_{out} , q_{side} , q_{long} are \mathbf{q} components in the outward, sideward and longitudinal direction. The λ parameter in the equations above determines correlation
 568 strength. The lambda parameter has values in the range $\lambda \in [-0.5, 1]$ and it depends on a pair type. In case of pairs of identical bosons (like $\pi\pi$ or KK) the
 569 lambda parameter $\lambda \rightarrow 1$. For identical fermions (e.g. $p-p$) $\lambda \rightarrow -0.5$. Values of
 570 λ observed experimentally are lower than 1 (for bosons) and greater than -0.5
 571 (for fermions). There are few explanations to this effect: detector efficiencies,
 572 inclusion of misidentified particles in a used sample or inclusion of non-correlated
 573 pairs (when one or both particles come from e.g. long-lived resonance). The
 574 analysis carried out in this work uses data from a model, therefore the detector
 575 efficiency and particle purity is not taken into account [25].
 576

578 3.2.5 Spherical harmonics decomposition of a correlation function

579 Results coming from an analysis using three-dimensional correlation function
 580 in Cartesian coordinates are quite difficult to visualize. To do that, one usually
 581 performs a projection into a one dimension in outward, sideward and longitudinal
 582 directions. One may loose important information about a correlation
 583 function in this procedure, because it gives only a limited view of the full three-
 584 dimensional structure. Recently, a more advanced way of presenting correlation
 585 function - a spherical harmonics decomposition, was proposed. The three-
 586 dimensional correlation function is decomposed into an infinite set of components
 587 in a form of one-dimensional histograms $C_l^m(q)$. In this form, a correlation
 588 function is defined as a sum of a series [26]:

$$C(\mathbf{q}) = \sum_{l,m} C_l^m(q) Y_l^m(\theta, \phi), \quad (3.20)$$

589 where $Y_l^m(\theta, \phi)$ is a spherical harmonic function. Spherical harmonics are an
 590 orthogonal set of solutions to the Laplace's equation in spherical coordinates
 591 Hence, in this approach, a correlation function is defined as a function of q , θ
 592 and ϕ . To obtain C_l^m coefficients in the series, one has to calculate the following
 593 integral:

$$C_l^m(q) = \int_{\Omega} C(q, \theta, \phi) Y_l^m(\theta, \phi) d\Omega, \quad (3.21)$$

594 where Ω is a full solid angle.

Spherical harmonics representation has several important advantages. The main advantage of this decomposition is that it requires less statistics than traditional analysis performed in Cartesian coordinates. Another one is that it encodes full three-dimensional information in a set of one-dimensional plots. In principle it does not have to be an advantage, because full description of a correlation function requires infinite number of l, m components. But it so happens that the intrinsic symmetries of a pair distribution in a femtoscopic analysis result in most of the components to vanish. For the identical particles correlation functions, all coefficients with odd values of l and m disappear. It has also been shown, that the most significant portion of femtoscopic data is stored in the components with the lowest l values. It is expected that, the main femtoscopic information is contained in the following components [25]:

$$C_0^0 \rightarrow R_{LCMS}, \quad (3.22)$$

$$\Re C_2^0 \rightarrow \frac{R_T}{R_{long}}, \quad (3.23)$$

$$\Re C_2^2 \rightarrow \frac{R_{out}}{R_{side}}, \quad (3.24)$$

595 where $R_{LCMS} = \sqrt{(R_{out}^2 + R_{side}^2 + R_{long}^2)/3}$ and $R_T = \sqrt{(R_{out}^2 + R_{side}^2)/2}$.

596 The C_0^0 is sensitive to the overall size of a correlation function. The $\Re C_2^0$ carries
 597 the information about the ratio of the transverse to the longitudinal radii, due
 598 to its $\cos^2(\theta)$ weighting in Y_2^0 . The component $\Re C_2^2$ with its $\cos^2(\phi)$ weighting
 599 encodes the ratio between outward and sideward radii. Thus, the spherical har-
 600 monics method allows to obtain and analyze full three-dimensional femtoscopic
 601 information from a correlation function [25].

602 3.3 Experimental approach

603 The correlation function is defined as a probability to observe two particles
 604 together divided by the product of probabilities to observe each of them sepa-
 605 rately (Eq. 3.16). Experimentally this is achieved by dividing two distributions
 606 of relative momentum of pairs of particles coming from the same event and the
 607 equivalent distribution of pairs where each particle is taken from different colli-
 608 sions. In this way, one obtains not only femtoscopic information but also all other
 609 event-wide correlations. This method is useful for experimentalists to estimate
 610 the magnitude of non-femtoscopic effects. There exists also a different approach,
 611 where two particles in pairs in the second distribution are also taken from the
 612 same event. The second method gives only information about physical effects
 613 accessible via femtoscopy. The aim of this work is a study of effects coming from
 614 two particle interferometry, hence the latter method was used.

615 In order to calculate experimental correlation function, one uses the follow-
 616 ing approach. One has to construct two histograms: the *numerator* N and the

617 denominator D with the particle pairs momenta, where particles are coming from
 618 the same event. Those histograms can be one-dimensional (as a function of $|\mathbf{q}|$),
 619 three dimensional (a function of three components of \mathbf{q} in LCMS) or a set of one-
 620 dimensional histogram representing components of the spherical harmonic de-
 621 composition of the distribution. The second histogram, D is filled for each pair
 622 with the weight 1.0 at a corresponding relative momentum $\mathbf{q} = 2\mathbf{k}^*$. The first one,
 623 N is filled with the same procedure, but the weight is calculated as $|\Psi_{ab}(\mathbf{r}^*, \mathbf{k}^*)|^2$.
 624 A division N/D gives the correlation function C . This procedure can be simply
 625 written as [25]:

$$C(\mathbf{k}^*) = \frac{N}{D} = \frac{\sum_{n_i \in D} \delta(\mathbf{k}^* i - \mathbf{k}^*) |\Psi_{ab}(\mathbf{r}^* i, \mathbf{k}^* i)|^2}{\sum_{n_i \in D} \delta(\mathbf{k}^* i - \mathbf{k}^*)} . \quad (3.25)$$

The D histogram represents the set of all particle pairs used in calculations.
 The n_i is a pair with the its relative momentum $\mathbf{k}^* i$ and relative separation $\mathbf{r}^* i$.
 The wave function used in Eq. 3.25 has one of the following forms:

$$|\Psi_{\pi\pi}(\mathbf{r}^*, \mathbf{k}^*)|^2 = |\Psi_{KK}(\mathbf{r}^*, \mathbf{k}^*)|^2 = 1 + \cos(2\mathbf{k}^* \mathbf{r}^*) , \quad (3.26)$$

$$|\Psi_{pp}(\mathbf{r}^*, \mathbf{k}^*)|^2 = 1 - \frac{1}{2} \cos(2\mathbf{k}^* \mathbf{r}^*) . \quad (3.27)$$

626 The first one is used in case of bosons, and the latter one is for identical fermi-
 627 ons. Mathematically, the procedure of calculating the Eq. 3.25 is equivalent to a
 628 calculation of an integral in Eq. 3.17 through a Monte-Carlo method.

629 3.4 Scaling of femtoscopic radii

630 In the hydrodynamic models describing expansion of a quark-gluon plasma,
 631 particles are emitted from the source elements. Each of the source elements is
 632 moving with the velocity u_μ given by hydrodynamic equations. Because solu-
 633 tions of those equations are smooth, nearby source elements have similar velo-
 634 cities. Each emitted particle from a certain source element is boosted with the
 635 flow velocity u_μ according to the point of origin. Hence particles emitted close
 636 to each other (pairs with large transverse momentum $|\mathbf{k}_T|$) will gain the similar
 637 velocity boost, they can combine into pairs with small relative momenta ($|\mathbf{q}|$) and
 638 therefore become correlated. If the two particles are emitted far away from each
 639 other (a pair with small $|\mathbf{k}_T|$), the flow field u_μ in their point of emission might
 640 be very different and it will be impossible for them to have sufficiently small rel-
 641 ative momenta in order to be in region of interference effect. This effect is visible
 642 in a width of a correlation function in the Fig. 3.4. The correlation function gets
 643 broader for greater values of $|\mathbf{k}_T|$ and the femtoscopic radius R becomes smal-
 644 ler [8, 27].

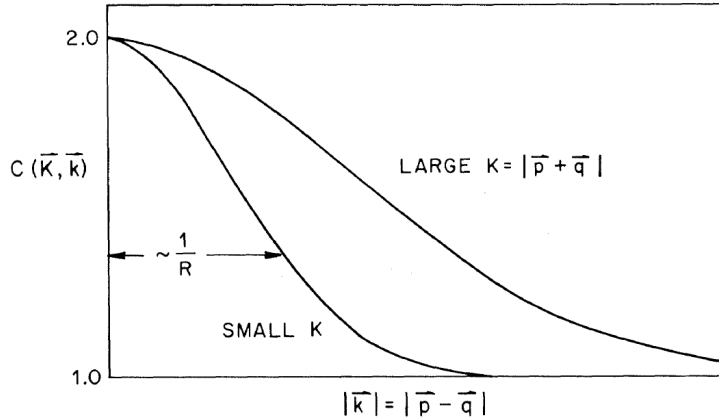


Figure 3.4: Correlation function width dependence on total pair momentum. Pion pairs with a large total momentum are more correlated [27].

645 3.4.1 Scaling in LCMS

Hydrodynamic calculations performed in LCMS show that femtoscopic radii in outward, sideward, and longitudinal direction show dependence on transverse mass $m_T = \sqrt{k_T^2 + m^2}$, where m is a mass of a particle [28]. Moreover, experimental results show that this scaling is observed for R_{LCMS} radii also. This dependence can be expressed as follows:

$$R_i = \alpha m_T^{-\beta} \quad (3.28)$$

646 where i subscript indicates that this equation applies to R_{out} , R_{side} and R_{long}
 647 radii. The β exponent is approximately equal 0.5. In case of strong transversal
 648 expansion of the emitting source, the decrease of longitudinal interferometry ra-
 649 dius can be more quick than $m_T^{-0.5}$, hence one can expect for longitudinal radii
 650 lower values of $\beta < 0.5$ [28].

651 3.4.2 Scaling in PRF

652 In the collisions at the LHC energies, pions are most abundant particles and
 653 their multiplicities are large enough to enable three-dimensional analysis. How-
 654 ever, for heavier particles, such as kaons and protons statistical limitations arise.
 655 Hence it is often possible to only measure one-dimensional radius R_{inv} for those
 656 particles. The R_{inv} is then calculated in the PRF. The transition from LCMS to
 657 PRF is a Lorentz boost in the direction of pair transverse momentum with velo-
 658 city $\beta_T = p_T/m_T$. Hence only R_{out} radius changes:

$$R_{out}^* = \gamma_T R_{out}. \quad (3.29)$$

659 The one-dimensional R_{inv} radius is direction-averaged source size in PRF. One
 660 can notice, that such power-law scaling of R_{inv} described by Eq. 3.28 is not

661 observed. To recover such scaling in PRF one has to take into consideration two
 662 effects when transforming variables from LCMS to PRF: overall radius growths
 663 and source distribution becomes non-Gaussian, while developing long-range
 664 tails (see Fig.3.3 for an example). The interplay of these two effects can be
 665 accounted with an approximate formula:

$$R_{inv} = \sqrt{(R_{out}^2 \sqrt{\gamma_T} + R_{side}^2 + R_{long}^2)/3} . \quad (3.30)$$

Assuming that all radii are equal $R_{out} = R_{side} = R_{long}$ this formula can be simplified:

$$R_{LCMS} \approx R_{inv} \times [(\sqrt{\gamma_T} + 2)/3]^{-1/2} . \quad (3.31)$$

666 This approximate formula allows to restore power-law behaviour of the scaled
 667 radii not only when the radii are equal, but also when their differences are small
 668 (for explanation see the last part of the section 3.2.3).

669 This method of recovering scaling in PRF can be used as a tool for the search
 670 of hydrodynamic collectivity between pions, kaons and protons in heavy ion col-
 671 lisions with the measurement of one-dimensional radius in PRF.

672 **Chapter 4**

673 **Results**

674 For the purposes of the femtoscopic analysis, events were generated using
675 THERMINATOR model for eight different sets of initial conditions correspond-
676 ing the following centrality ranges: 0-5%, 0-10%, 10-20%, 20-30%, 30-40%, 40-
677 50%, 50-60% and 60-70% for the Pb-Pb collisions at the centre of mass energy
678 $\sqrt{s_{NN}} = 2.76 \text{ TeV}$.

679 **4.1 Identical particles correlations**

680 The correlation functions (three-dimensional and one-dimensional) were cal-
681 culated separately for the following different pairs of identical particles: $\pi-\pi$, $K-$
682 K and $p-p$ for nine k_T bins (in GeV/c): 0.1-0.2, 0.2-0.3, 0.3-0.4, 0.4-0.5, 0.6-0.7,
683 0.7-0.8, 0.8-1.0 and 1.0-1.2. In case of kaons, k_T ranges start from 0.3 and for pi-
684 ons from 0.4 and for both of them the maximum value is 1.0. The k_T ranges for
685 the heavier particles were limited to maintain sufficient multiplicity to perform
686 reliable calculations.

687 **4.1.1 Spherical harmonics components**

688 The three-dimensional correlation functions as functions of relative
689 momentum q_{LCMS} were calculated in a form of spherical harmonics components
690 series accordingly to the Eq. 3.21. In the femtoscopic analysis of identical
691 particles, the most important information is stored in the $\Re C_0^0$, $\Re C_2^0$ and $\Re C_2^2$.
692 Correlation functions obtained in this procedure for different centrality bins for
693 the pairs of pions, kaons and protons are presented in the Fig. 4.1, 4.2 and 4.3.

694 Coefficients for pairs of identical bosons (pions and kaons) are shown in the
695 Fig. 4.1 and 4.2. The increase of a correlation in the low momenta regime is clearly
696 visible in the $\Re C_0^0$ component and has its source in the Bose-Einstein statistics.
697 The $\Re C_0^0$ resembles one-dimensional correlation function and in fact it encodes
698 information about overall source radius. The second coefficient $\Re C_2^0$ differs from
699 zero (is negative), which yields the information about the ratio R_T/R_{long} . The

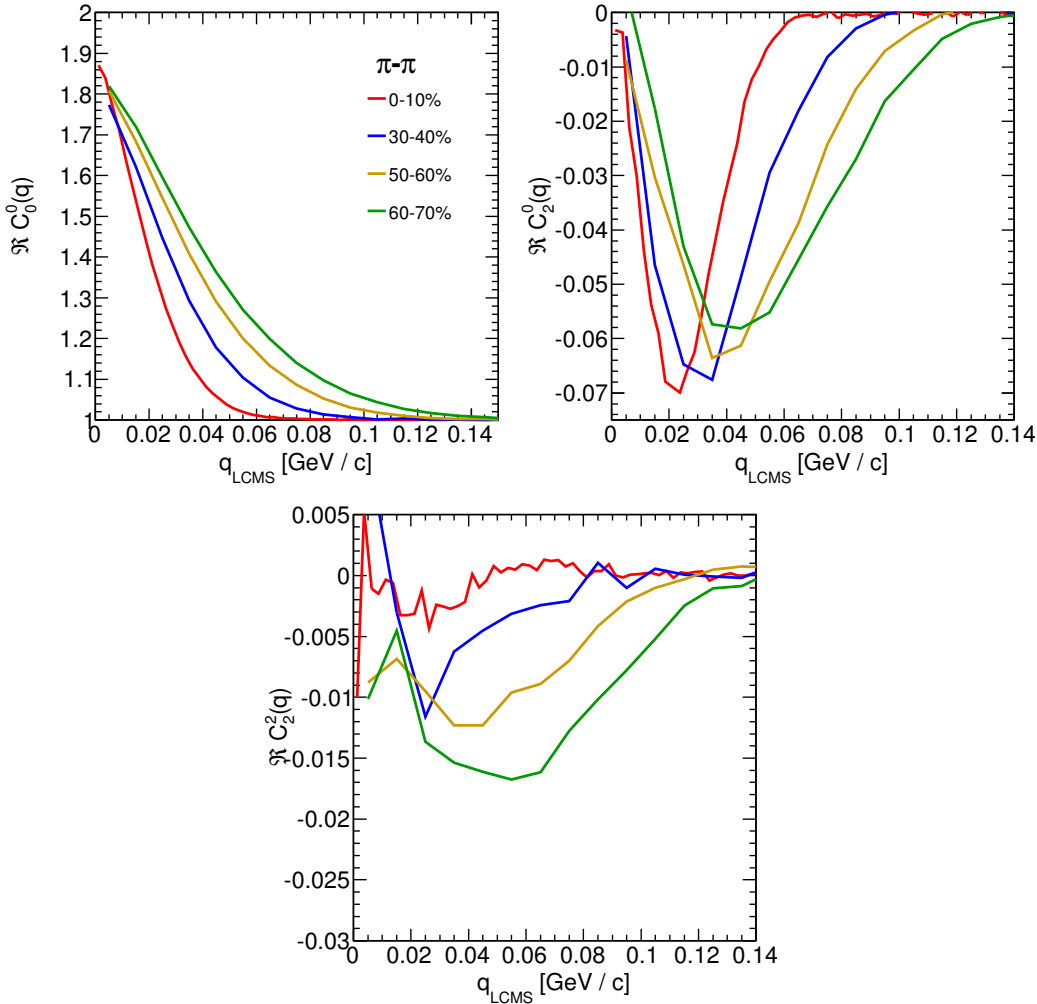


Figure 4.1: Spherical harmonics coefficients of the two-pion correlation function. From the top left: $\Re C_0^0$, $\Re C_2^0$ and $\Re C_2^2$. Only few centrality bins are presented for increased readability.

700 $\Re C_2^2$ stores the R_{out}/R_{side} ratio and one can notice that it is non-vanishing (is also
701 negative).

702 The correlation function for a pair of identical fermions is in the Fig. 4.3. An
703 influence of Fermi-Dirac statistics has its effect in the decrease of a correlation
704 down to 0.5 at low relative momentum, which can be observed in $\Re C_0^0$. The $\Re C_2^0$
705 and $\Re C_2^2$ coefficients differ from zero and become positive.

706 The common effect for the spherical harmonics form of a correlation function
707 is the “mirroring” of the shape of the $\Re C_0^0$ coefficient - when correlation function
708 decreases, the $\Re C_2^0$ and $\Re C_2^2$ are becoming positive and vice versa. This is quite
709 different behaviour than in the case of correlations of non-identical particles,

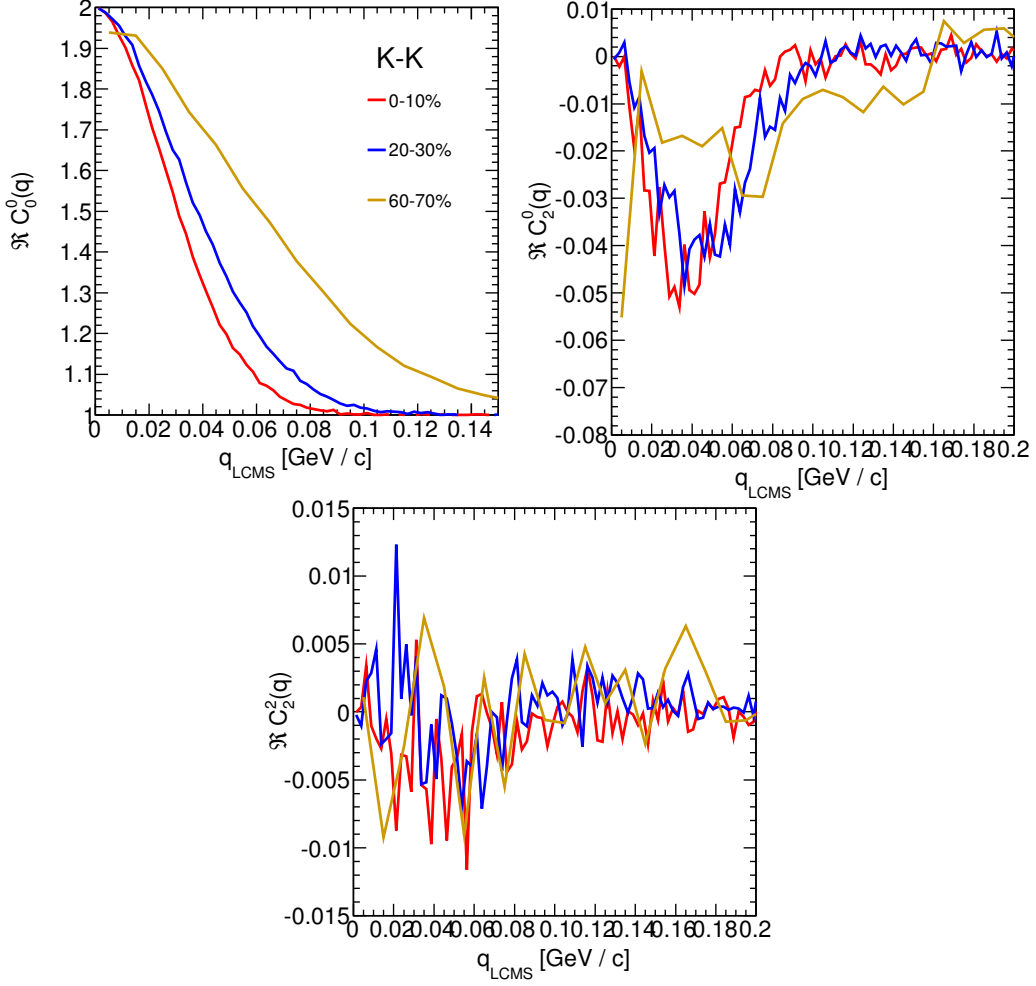


Figure 4.2: Spherical harmonics coefficients of the two-kaon correlation function. From the top left: $\Re C_0^0$, $\Re C_2^0$ and $\Re C_2^2$. Only few centrality bins are presented for increased readability. The $\Re C_2^2$ is noisy, but one can still notice that it differs from zero and is becoming negative.

710 where the $\Re C_2^0$ still behaves in the same manner, but $\Re C_2^2$ has the opposite sign
 711 to the $\Re C_2^0$ [25].

712 In all cases, the correlation function gets wider with the peripherality of a
 713 collision i.e. the correlation function for most central collisions (0-10%) is much
 714 narrower than for the most peripheral ones (60-70%). This phenomena is clearly
 715 visible the $\Re C_0^0$ coefficients. Other components are also affected by this effect,
 716 this is especially noticeable in the case of kaons and pions. For the protons, the
 717 results are noisy, hence this effect is not distinguishable.

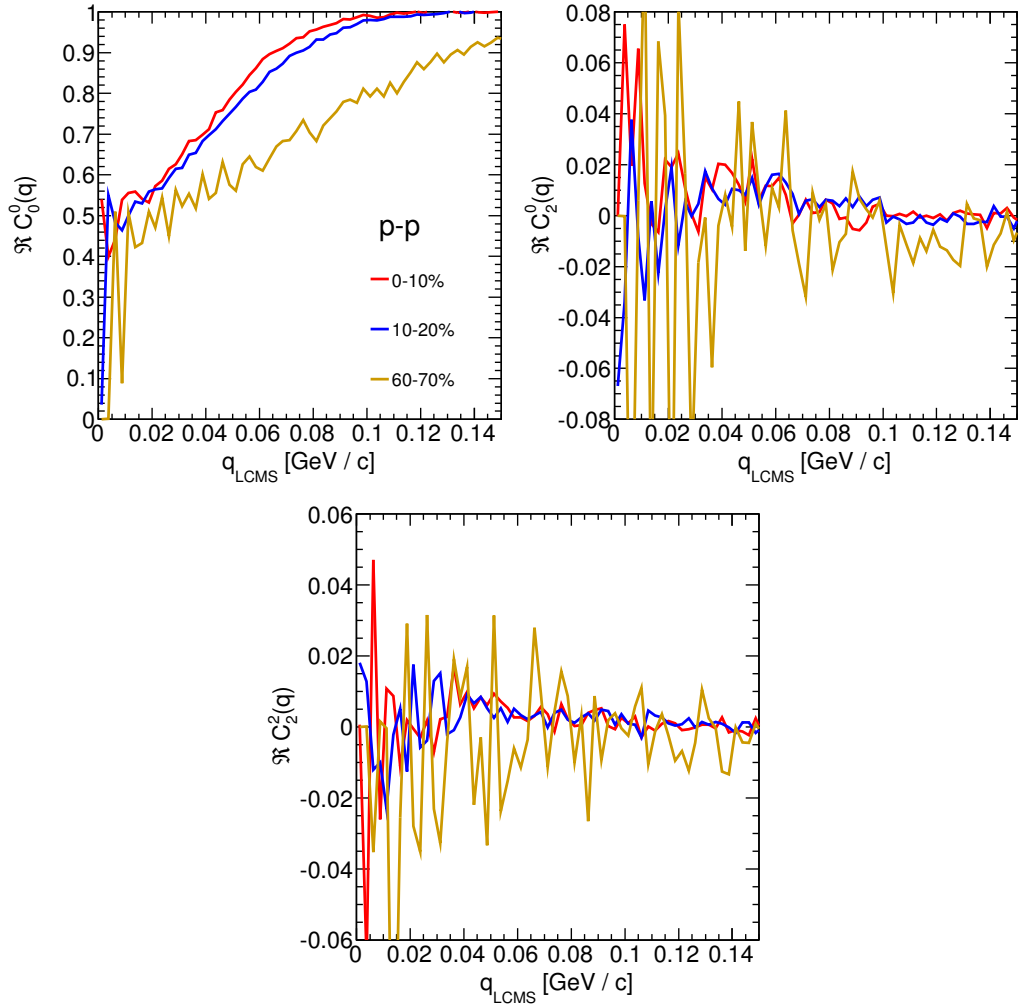


Figure 4.3: Spherical harmonics coefficients of the two-proton correlation function. From the top left: $\Re C_0^0$, $\Re C_2^0$ and $\Re C_2^2$. Only few centrality bins are presented for increased readability. The $\Re C_2^0$ and $\Re C_2^2$ are noisy, but one can still notice, that they differ from zero and are becoming positive.

718 **4.1.2 Centrality dependence of a correlation function**

719 The centrality dependence of a correlation function is especially visible in
 720 one-dimensional correlation functions. This effect is presented in the Fig. 4.4 -
 721 the width is smaller in the most central collisions. Hence, the femtoscopic radii
 722 (proportional to the inverse of width) is increasing with the centrality. An ex-
 723 planation for this growth is that in the most central collisions, a size of a created
 system is larger than for the peripheral ones.

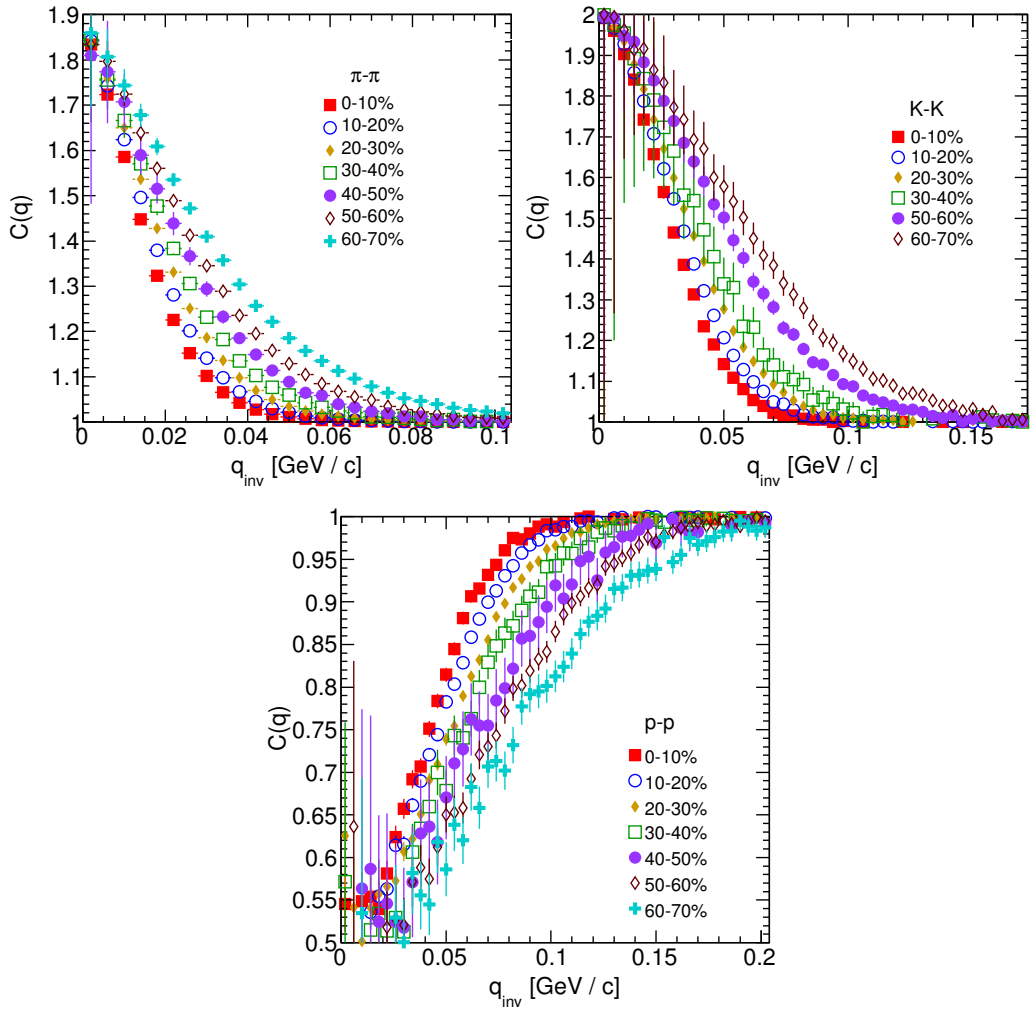


Figure 4.4: One-dimensional correlation function for pions, kaons and protons for different centralities.

725 **4.1.3 k_T dependence of a correlation function**

726 In the Fig. 4.5 there are presented one-dimensional correlation functions for
 727 pions, kaons and protons for the same centrality bin, but different k_T ranges. One
 728 can observe in all cases of the particle types, appearance of the same trend: with
 729 the increase of the total transverse momentum of a pair, the width of a correlation
 730 function increases and the femtoscopic radius decreases. The plots in the Fig. 4.5
 731 were zoomed in to show the influence of k_T .

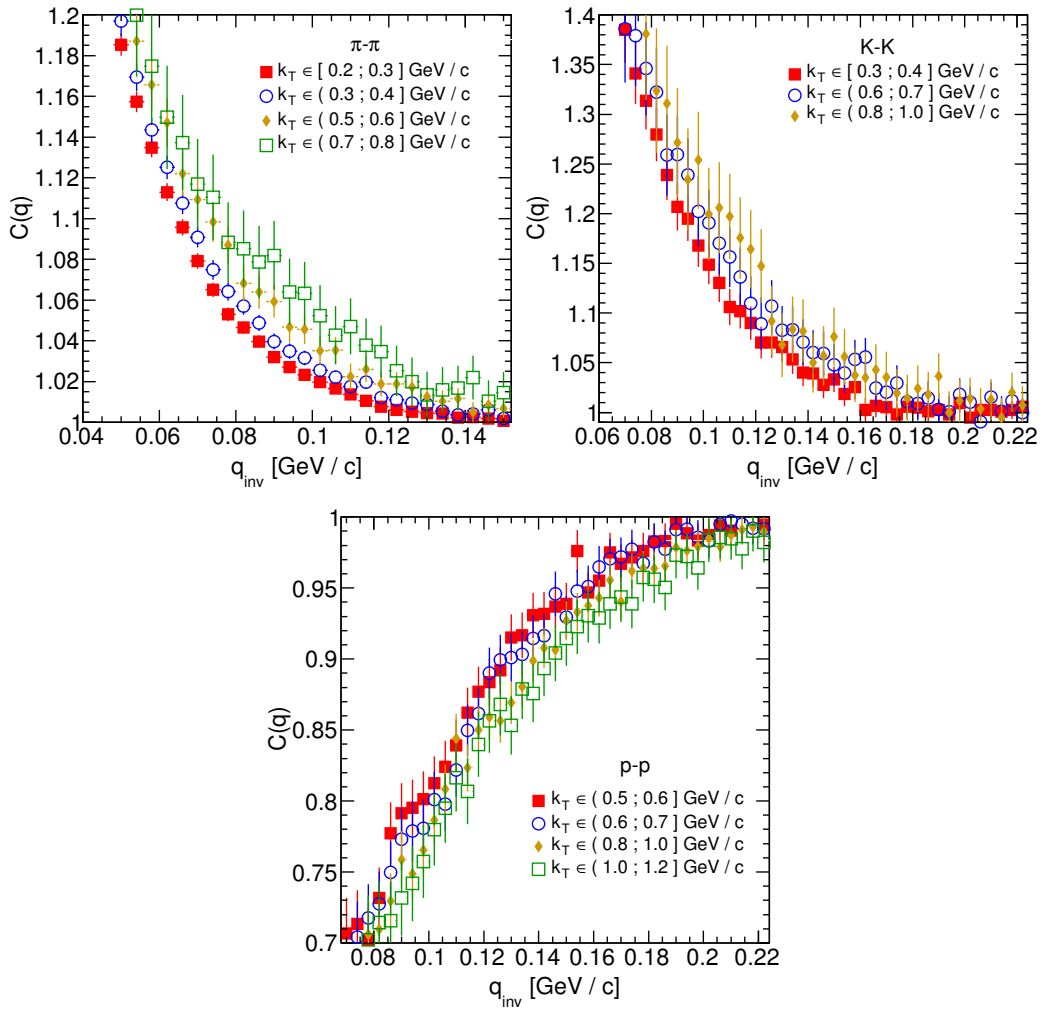


Figure 4.5: One-dimensional correlation functions for pions, kaons and protons, for the same centrality bin and different k_T ranges. The plot was zoomed in to the region which illustrates the k_T dependence in the best way. Only few of the calculated ranges are presented for better readability.

4.2 Results of the fitting procedure

In order to perform a quantitative analysis of a wide range of correlation functions, the theoretical formulas were fitted to the calculated experimental-like data. In this procedure, the femtoscopic radii for the three-dimensional as well as one-dimensional correlation functions were extracted.

4.2.1 Femtoscopic radii scaling with the transverse mass

The main goal of this analysis is a verification of a transverse mass scaling of different particles types. The radii are plotted as a function of a transverse mass $m_T = \sqrt{k_T^2 + m^2}$ and the following power-law is fitted:

$$R_x = \alpha m_T^{-\beta}, \quad (4.1)$$

where the α and β are free parameters.

In the Fig. 4.12 there are femtoscopic radii in the outward, sideward and longitudinal direction of the analysis of two-pion correlation functions in LCMS. The

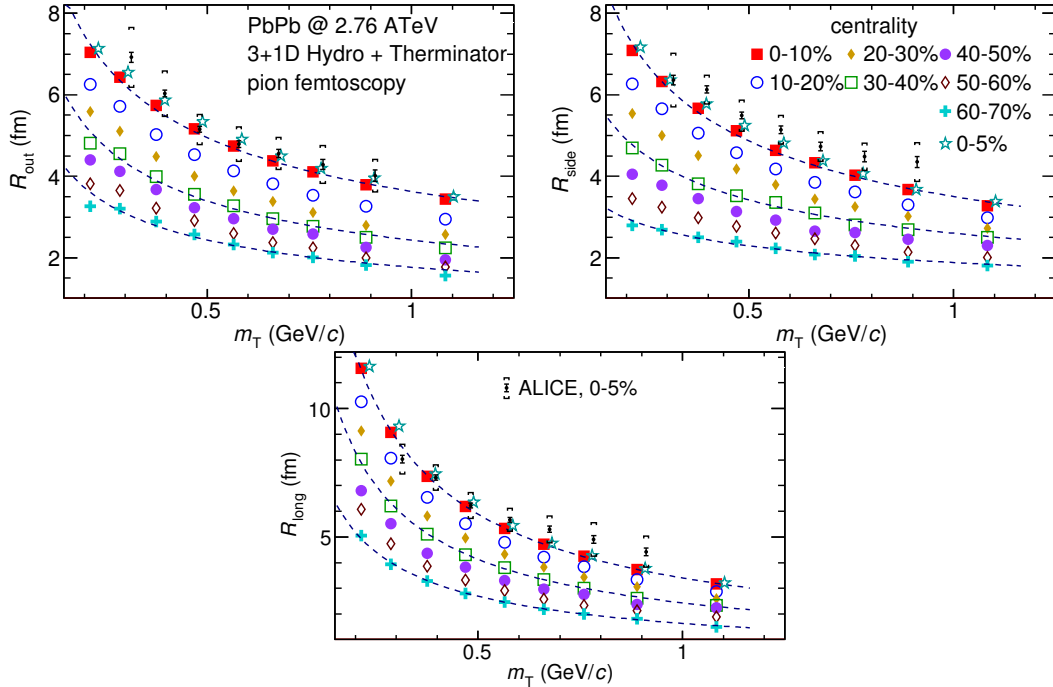


Figure 4.6: Femtoscopic radii in LCMS for all centrality bins as a function of m_T . The dashed lines are power-law fits. The most central collisions (0-5%) are compared to the results from ALICE [29]. The two datasets are shifted to the right for visibility [30].

744 dashed lines are fits of the power law to the data. The results for the top 5% cent-
 745 ral collisions (star-shaped markers in the Fig. 4.12) are with the good agreement
 746 with the experimental data from ALICE [29].

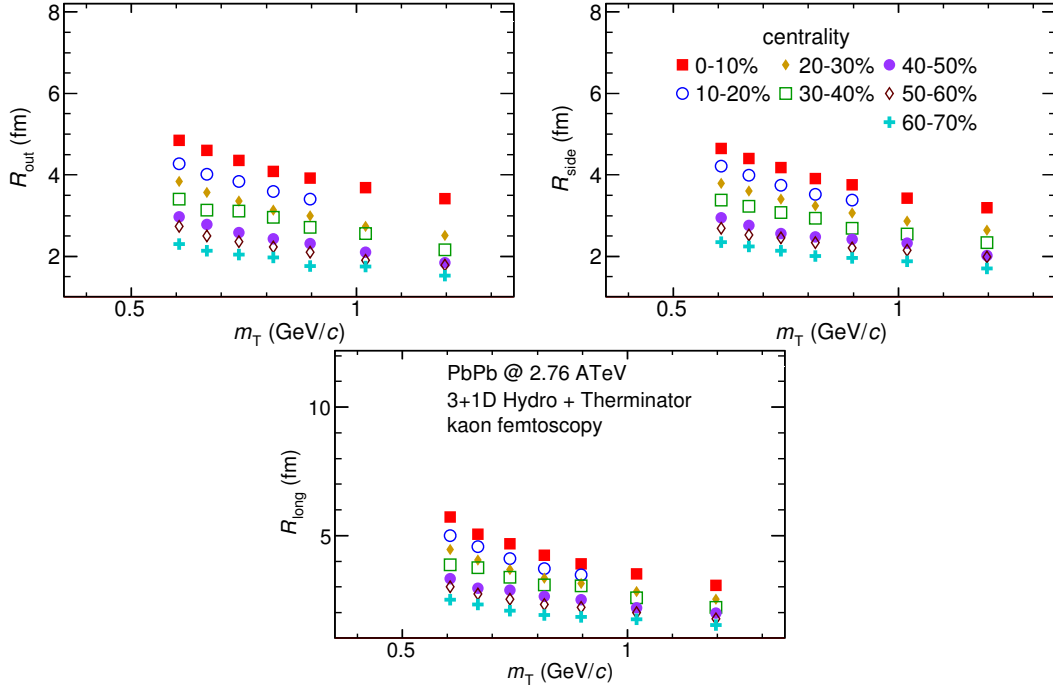


Figure 4.7: no caption [30].

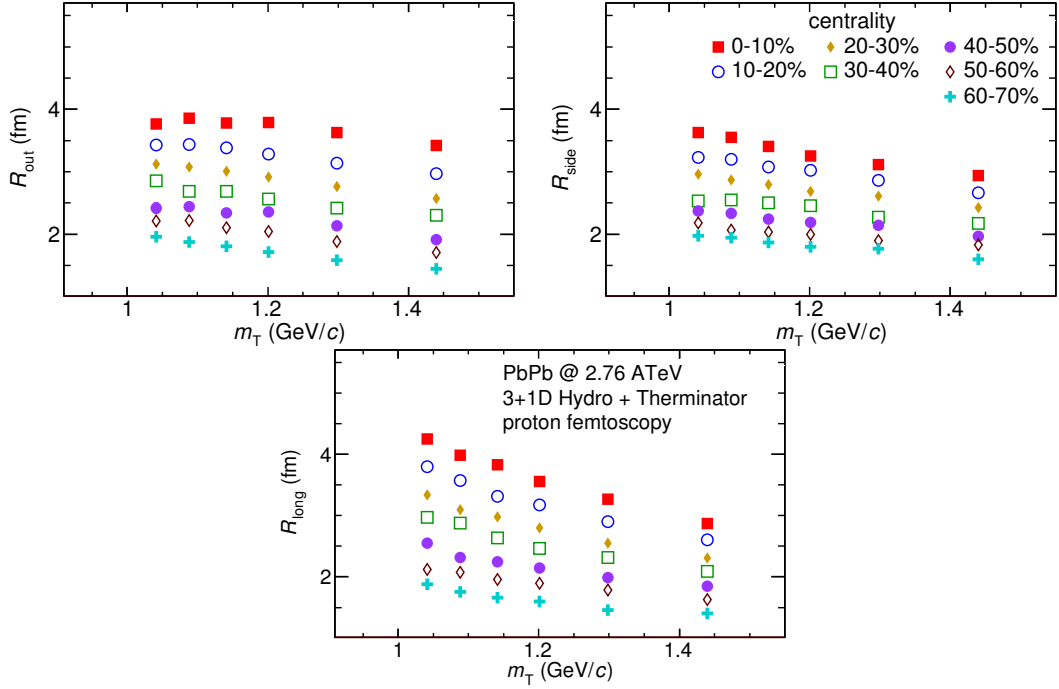


Figure 4.8: no caption [30].

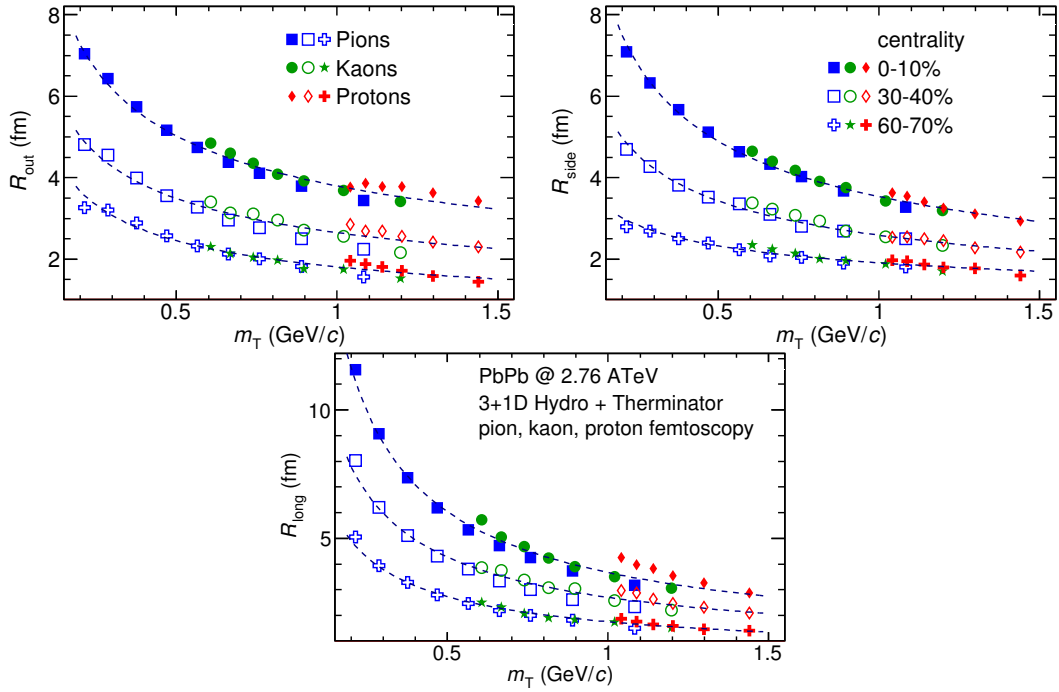


Figure 4.9: no caption [30].

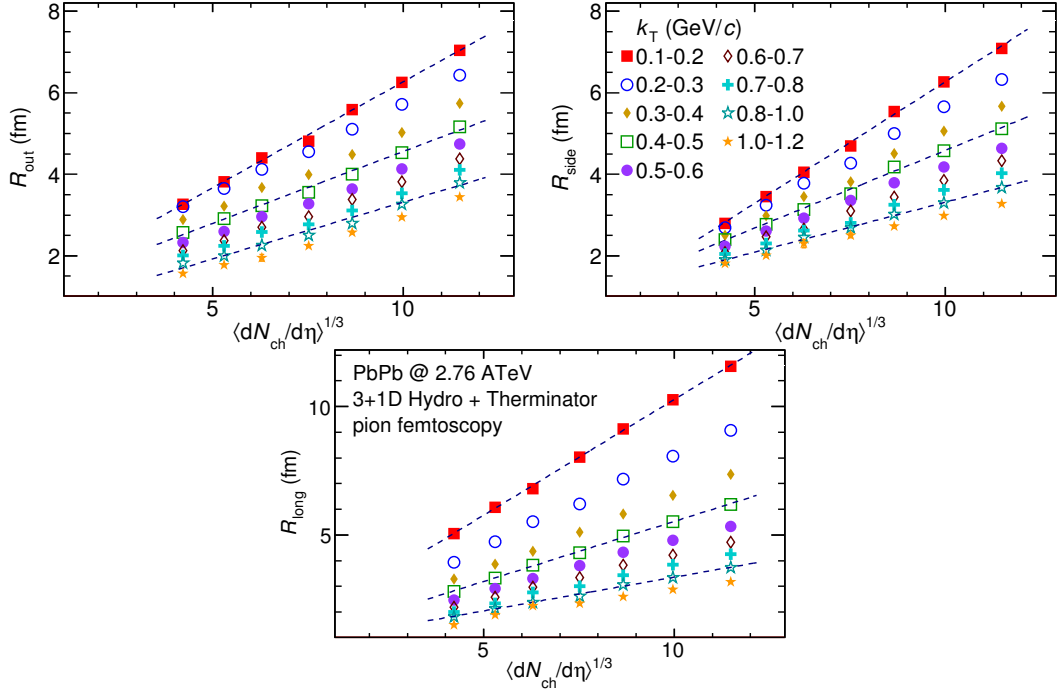


Figure 4.10: no caption [30].

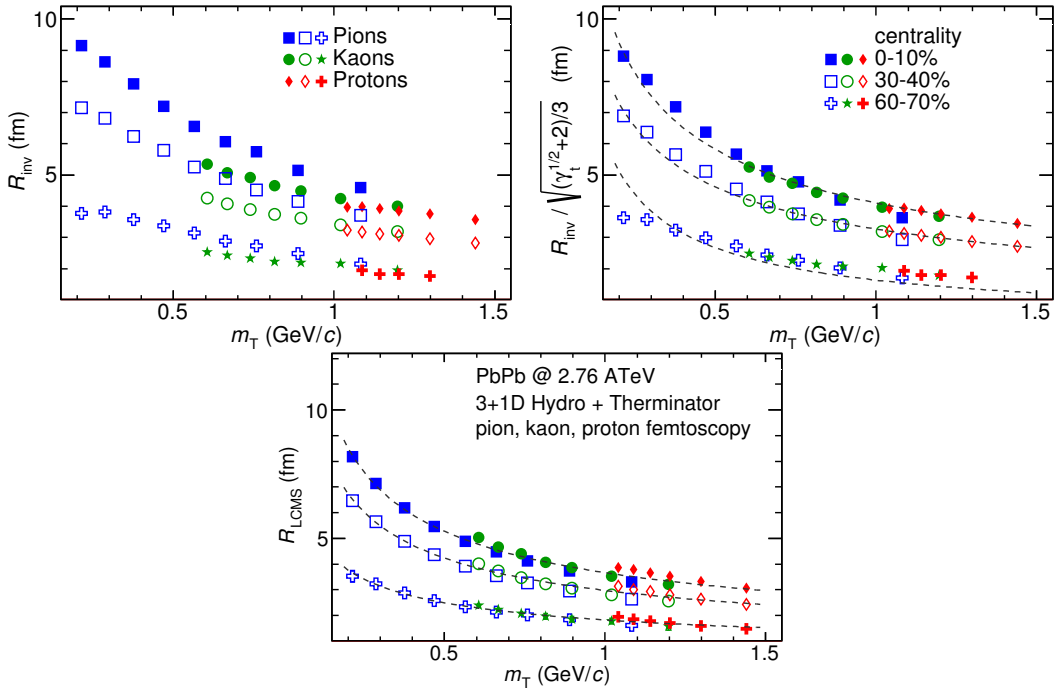


Figure 4.11: no caption [30].

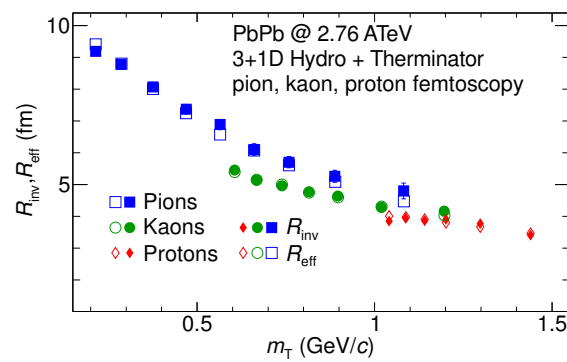


Figure 4.12: no caption [30].

⁷⁴⁷ **4.3 Discussion of results**

⁷⁴⁸ **Chapter 5**

⁷⁴⁹ **Summary**

Bibliography

- [1] Standard Model of Elementary Paticles - Wikipedia, the free encyclopedia
http://en.wikipedia.org/wiki/standard_model.
- [2] R. Aaij et al. (LHCb Collaboration). Observation of the resonant character of the $z(4430)^-$ state. *Phys. Rev. Lett.*, 112:222002, Jun 2014.
- [3] Donald H. Perkins. *Introduction to High Energy Physics*. Cambridge University Press, fourth edition, 2000. Cambridge Books Online.
- [4] G. Odyniec. *Phase Diagram of Quantum Chromo-Dynamics* - course at Faculty of Physics, Warsaw University of Technology, Jun 2012.
- [5] J. Beringer et al. (Particle Data Group). The Review of Particle Physics. *Phys. Rev.*, D86:010001, 2012.
- [6] Z. Fodor and S.D. Katz. The Phase diagram of quantum chromodynamics. 2009.
- [7] F. Karsch. Lattice results on QCD thermodynamics. *Nuclear Physics A*, 698(1-4):199 – 208, 2002.
- [8] Adam Kisiel. *Studies of non-identical meson-meson correlations at low relative velocities in relativistic heavy-ion collisions registered in the STAR experiment*. PhD thesis, Warsaw University of Technology, Aug 2004.
- [9] J. Bartke. *Relativistic Heavy Ion Physics*. World Scientific Pub., 2009.
- [10] W. Florkowski. *Phenomenology of Ultra-Relativistic Heavy-Ion Collisions*. World Scientific, 2010.
- [11] Science Grid This Week, October 25, 2006 - Probing the Perfect Liquid with the STAR Grid
http://www.interactions.org/sgtw/2006/1025/star_grid_more.html.
- [12] K. Grebieszkow. Fizyka zderzeń ciężkich jonów,
<http://www.if.pw.edu.pl/~kperl/hip/hip.html>.
- [13] Ulrich W. Heinz. From SPS to RHIC: Maurice and the CERN heavy-ion programme. *Phys. Scripta*, 78:028005, 2008.

- 778 [14] J. Adams et al. Identified particle distributions in pp and Au+Au collisions
779 at $s(\text{NN})^{**}(1/2) = 200 \text{ GeV}$. *Phys.Rev.Lett.*, 92:112301, 2004.
- 780 [15] G. David, R. Rapp, and Z. Xu. Electromagnetic Probes at RHIC-II. *Phys.Rept.*,
781 462:176–217, 2008.
- 782 [16] A. Marin et al. Dilepton measurements with CERES. *PoS*, CPOD07:034,
783 2007.
- 784 [17] J. Adams et al. Experimental and theoretical challenges in the search for the
785 quark gluon plasma: The STAR Collaboration’s critical assessment of the
786 evidence from RHIC collisions. *Nucl.Phys.*, A757:102–183, 2005.
- 787 [18] Adam Kisiel, Tomasz Taluc, Wojciech Broniowski, and Wojciech
788 Florkowski. THERMINATOR: THERMal heavy-IoN generATOR. *Comput.Phys.Commun.*, 174:669–687, 2006.
- 790 [19] Mikolaj Chojnacki, Adam Kisiel, Wojciech Florkowski, and Wojciech Bro-
791 niowski. THERMINATOR 2: THERMal heavy IoN generATOR 2. *Comput.Phys.Commun.*, 183:746–773, 2012.
- 793 [20] I. et al (BRAHMS Collaboration) Bearden. Charged meson rapidity distri-
794 butions in central Au + Au collisions at $\sqrt{s_{\text{NN}}} = 200 \text{ GeV}$. *Phys. Rev. Lett.*,
795 94:162301, Apr 2005.
- 796 [21] W. Israel and J.M. Stewart. Transient relativistic thermodynamics and kin-
797 etic theory. *Annals of Physics*, 118(2):341 – 372, 1979.
- 798 [22] Piotr Bożek. Flow and interferometry in (3 + 1)-dimensional viscous hydro-
799 dynamics. *Phys. Rev. C*, 85:034901, Mar 2012.
- 800 [23] K. Kovtun, P. D. T. Son, and A. O. Starinets. Viscosity in strongly interacting
801 quantum field theories from black hole physics. *Phys. Rev. Lett.*, 94:111601,
802 Mar 2005.
- 803 [24] Fred Cooper and Graham Frye. Single-particle distribution in the hydro-
804 dynamic and statistical thermodynamic models of multiparticle production.
805 *Phys. Rev. D*, 10:186–189, Jul 1974.
- 806 [25] Adam Kisiel. Nonidentical-particle femtoscopy at $\sqrt{s_{\text{NN}}} = 200 \text{ GeV}$ in hy-
807 drodynamics with statistical hadronization. *Phys. Rev. C*, 81:064906, Jun
808 2010.
- 809 [26] Adam Kisiel and David A. Brown. Efficient and robust calculation of femto-
810 scopic correlation functions in spherical harmonics directly from the raw
811 pairs measured in heavy-ion collisions. *Phys.Rev.*, C80:064911, 2009.
- 812 [27] S. Pratt. Pion Interferometry for Exploding Sources. *Phys.Rev.Lett.*, 53:1219–
813 1221, 1984.

- 814 [28] S.V. Akkelin and Yu.M. Sinyukov. The HBT-interferometry of expanding
815 inhomogeneous sources. *Z.Phys.*, C72:501–507, 1996.
- 816 [29] K. Aamodt et al. Two-pion Bose-Einstein correlations in central Pb-Pb colli-
817 sions at $\sqrt{s_{NN}} = 2.76$ TeV. *Phys.Lett.*, B696:328–337, 2011.
- 818 [30] A. Kisiel, M. Galazyn, and P. Bozek. Pion, kaon, and proton femtoscopy in
819 Pb–Pb collisions at $\sqrt{s_{NN}}=2.76$ TeV modeled in 3+1D hydrodynamics. 2014.

List of Figures

| | | |
|------|--|----|
| 1.1 | The Standard Model of elementary particles [1]. | 2 |
| 1.2 | A string break and a creation of a pair quark-anti-quark [4]. | 4 |
| 1.3 | The coupling parameter α_s dependence on four-momentum transfer Q^2 [5]. | 5 |
| 1.4 | The QCD potential for a pair quark-antiquark as a function of distance for different temperatures. A value of a potential decreases with the temperature [4]. | 5 |
| 1.5 | A number of degrees of freedom as a function of a temperature [7]. | 6 |
| 1.6 | Phase diagram coming from the Lattice QCD calculations [8]. | 7 |
| 1.7 | Left: stages of a heavy ion collision simulated in the UrQMD model. Right: schematic view of a heavy ion collision evolution [8]. | 8 |
| 1.8 | Overlapping region which is created in heavy ion collisions has an almond shape. Visible x-z plane is a <i>reaction plane</i> . The x-y plane is a <i>transverse plane</i> . The z is a direction of the beam [11]. | 10 |
| 1.9 | Cross-section of a heavy ion collision in a transverse plane. Ψ_R is an angle between transverse plane and the reaction plane. The b parameter is an <i>impact parameter</i> - a distance between centers of nuclei during a collision. An impact parameter is related with the centrality of a collision and a volume of the quark-gluon plasma [12]. | 11 |
| 1.10 | <i>Lower:</i> The elliptic flow v_2 follows the hydrodynamical predictions for an ideal fluid perfectly. Note that > 99% of all final hadrons have $p_T < 1.5 \text{ GeV}/c$. <i>Upper left:</i> The v_2 plotted versus transverse kinetic energy $KE_T = m_T - m_0 = \sqrt{p_T^2 + m_0^2} - m_0$. The v_2 follows different universal curves for mesons and baryons. <i>Upper right:</i> When scaled by the number of valence quarks, the v_2 follows the same universal curve for all hadrons and for all values of scaled transverse kinetic energy [13]. | 12 |
| 1.11 | Invariant yield of particles versus transverse mass $m_T = \sqrt{p_T^2 + m_0^2}$ for π^\pm , K^\pm , p and \bar{p} at mid-rapidity for p+p collisions (bottom) and Au+Au events from 70-80% (second bottom) to 0-5% (top) centrality [14]. | 13 |

| | | |
|-----|--|----|
| 852 | 1.12 Thermal photons spectra for the central Au+Au collisions at $\sqrt{s_{NN}} = 200$ GeV at computed within different hydrodynamical models compared with the pQCD calculations (solid line) and experimental data from PHENIX (black dots) [15]. | 14 |
| 853 | | |
| 854 | | |
| 855 | | |
| 856 | 1.13 Left: Invariant mass spectrum of e^+e^- pairs in Pb+Au collisions at 158A GeV compared to the sum coming from the hadron decays predictions. Right: The expectations coming from model calculations assuming a dropping of the ρ mass (blue) or a spread of the ρ width in the medium (red) [16]. | 15 |
| 857 | | |
| 858 | | |
| 859 | | |
| 860 | | |
| 861 | 1.14 Azimuthal angle difference $\Delta\phi$ distributions for different colliding systems at $\sqrt{s_{NN}} = 200$ GeV. Transverse momentum cut: $p_T > 2$ GeV. For the Au+Au collisions the away-side jet is missing [17]. . . | 16 |
| 862 | | |
| 863 | | |
| 864 | 3.1 Bertsch-Pratt direction naming convention used in heavy ion collision. | 22 |
| 865 | | |
| 866 | 3.2 The pair wave function is a superposition of all possible states. In case of particle interferometry it includes two cases: particles with momenta p_1, p_2 registered by detectors A, B and p_1, p_2 registered by B, A respectively. | 23 |
| 867 | | |
| 868 | | |
| 869 | | |
| 870 | 3.3 An averaged three-dimensional Gaussian source function with different widths was averaged into one-dimensional function. To illustrate deformations, one-dimensional Gaussian distribution was fitted. | 26 |
| 871 | | |
| 872 | | |
| 873 | | |
| 874 | 3.4 Correlation function width dependence on total pair momentum. Pion pairs with a large total momentum are more correlated [27]. . | 30 |
| 875 | | |
| 876 | 4.1 Spherical harmonics coefficients of the two-pion correlation function. From the top left: $\Re C_0^0$, $\Re C_2^0$ and $\Re C_2^2$. Only few centrality bins are presented for increased readability. | 33 |
| 877 | | |
| 878 | | |
| 879 | 4.2 Spherical harmonics coefficients of the two-kaon correlation function. From the top left: $\Re C_0^0$, $\Re C_2^0$ and $\Re C_2^2$. Only few centrality bins are presented for increased readability. The $\Re C_2^2$ is noisy, but one can still notice that it differs from zero and is becoming negative. | 34 |
| 880 | | |
| 881 | | |
| 882 | | |
| 883 | 4.3 Spherical harmonics coefficients of the two-proton correlation function. From the top left: $\Re C_0^0$, $\Re C_2^0$ and $\Re C_2^2$. Only few centrality bins are presented for increased readability. The $\Re C_2^0$ and $\Re C_2^2$ are noisy, but one can still notice, that they differ from zero and are becoming positive. | 35 |
| 884 | | |
| 885 | | |
| 886 | | |
| 887 | | |
| 888 | 4.4 One-dimensional correlation function for pions, kaons and protons for different centralities. | 36 |
| 889 | | |

| | | |
|---|--|----|
| 890 4.5 | One-dimensional correlation functions for pions, kaons and pro- | |
| 891 tons, for the same centrality bin and different k_T ranges. The plot | | |
| 892 was zoomed in to the region which illustrates the k_T dependence | | |
| 893 in the best way. Only few of the calculated ranges are presented | | |
| 894 for better readability. | | 37 |
| 895 4.6 | Femtoscopic radii in LCMS for all centrality bins as a function of | |
| 896 m_T . The dashed lines are power-law fits. The most central colli- | | |
| 897 sions (0-5%) are compared to the results from ALICE [29]. The two | | |
| 898 datasets are shifted to the right for visibility [30]. | | 38 |
| 899 4.7 | no caption [30]. | 39 |
| 900 4.8 | no caption [30]. | 40 |
| 901 4.9 | no caption [30]. | 40 |
| 902 4.10 | no caption [30]. | 41 |
| 903 4.11 | no caption [30]. | 41 |
| 904 4.12 | no caption [30]. | 42 |